

DEMNUi: cross-correlating the nonlinear ISWRS effect with CMB-lensing and galaxies in the presence of massive neutrinos

Viviana Cuozzo^{a,b} Carmelita Carbone^c Matteo Calabrese^d
Elisabetta Carella^{c,e} and Marina Migliaccio^{a,b}

^aUniversità degli Studi di Roma Tor Vergata, via della Ricerca Scientifica 1, I-00133 Roma, Italy

^bINFN, Sezione di Roma 2, Università degli Studi di Roma Tor Vergata, via della Ricerca Scientifica 1, I-00133 Roma, Italy

^cINAF – Istituto di Astrofisica Spaziale e Fisica cosmica di Milano (IASF-MI), via Alfonso Corti 12, I-20133 Milano, Italy

^dAstronomical Observatory of the Autonomous Region of the Aosta Valley (OAVdA), Loc. Lignan 39, I-11020, Nus (Aosta Valley), Italy

^eDipartimento di Fisica “Aldo Pontremoli”, Università degli Studi di Milano, via Celoria 16, I-20133 Milano, Italy

E-mail: vcuozzo@roma2.infn.it

Abstract. We present a novel analytical approach to study the cross-correlations between the Integrated Sachs Wolfe–Rees Sciama (ISWRS) effects and large-scale structure tracers in the presence of massive neutrinos. Our method has been validated against large N-body simulations with a massive neutrino particle component, namely the DEMNUi suite. We investigate the impact of different neutrino masses on the cross-correlations between ISWRS and both Cosmic Microwave Background (CMB) lensing and galaxies. We show that the position of the sign inversion due to nonlinear effects is strongly related to the neutrino mass. While such nonlinear cross-correlation signals may not be able alone to constrain the neutrino mass, our approach paves the way for future studies to detect the amplitude of these cross-spectra on small scales, and to explore the combined impact of dark energy and neutrino mass from future galaxy surveys and CMB experiments.

Contents

1	Introduction	1
2	The Integrated Sachs Wolfe and the Rees Sciama effects	3
3	Nonlinear modelling with N-body simulations	6
3.1	The Dark Energy and Massive Neutrino Universe simulations	6
3.2	Map-making procedure: ISWRS and CMB-lensing	8
3.2.1	Simulated ISWRS and CMB-lensing auto-spectra	8
3.3	Map-making procedure: projected galaxy mocks	8
3.3.1	Galaxy bias and selection function from DEMNUni simulations	9
3.3.2	Simulated projected galaxy auto-spectra	12
4	The ISWRS cross-correlation with the CMB-lensing potential	14
5	The ISWRS cross-correlation with galaxies	14
5.1	Nonlinear ISWRS-galaxy cross-spectra: effects of different bias modellings	16
5.1.1	Massive neutrino impact on the scale-independent bias	18
5.1.2	Scale-independent and scale-dependent bias effects in the neutrino massless neutrino case	18
5.2	Nonlinear ISWRS-galaxy cross-spectra: detecting the neutrino mass	19
5.3	Nonlinear ISWRS-galaxy cross-spectra: the case of different galaxy surveys	20
6	Conclusions	22
A	Test nonlinearities in the dark matter power spectra	29
B	Cosmic Variance (massless neutrino case)	29

1 Introduction

Since its discovery in 1965 [1], the Cosmic Microwave Background (CMB) has provided the most significant evidence for the Big Bang Theory and the study of its anisotropies has given us a unique window onto the primordial Universe. Measurements from WMAP [2–4] and Planck [5–7] have consistently been in line with the predictions of the Λ CDM model, the so-called Standard Cosmological Model, and have been fundamental in inferring constraints on the cosmological parameters that characterise it. However, there are still many open questions in cosmology, and several tensions exist in the Standard Cosmological Model. One of the most investigated topics today is the nature of Dark Energy (DE), which appears to dominate the energy density of the Universe at late times (see eg [8]), counteracting the gravitational collapse and inducing a background accelerated expansion. Another example is the value of the sum of the three neutrino masses, $M_\nu = \sum m_\nu$, whose best bounds come from cosmological data [7, 9, 10].

Among several cosmological probes, both these issues can be addressed also by measuring and analysing the late Integrated Sachs Wolfe (ISW) effect [11], which is the temperature variation that CMB photons experience when they propagate in a time-varying gravitational

potential, and the Rees Sciama (RS) effect [12], which is its nonlinear counterpart. DE is mainly responsible for the combined ISWRS signal, but it is not the unique source of such effects. The presence of massive neutrinos induces a slow decay of the gravitational potential [13] that generates ISWRS even in the absence of a background expansion. Therefore, a full reconstruction of the ISWRS effect would provide new information on the physics of neutrinos and of DE, allowing to help constraining the DE Equation of State (EoS) and the total neutrino mass. However, in this respect there has not been much progress as this signal is extremely faint compared to CMB primary anisotropies. Moreover, these measurements are limited in the linear regime by cosmic variance and in the nonlinear regime by the lack of data. The only way to reconstruct the ISWRS is to use its cross-correlation with the Large Scale Structure (LSS), in order to exploit the tracers that follow the dark matter field and the variation of the gravitational potential produced by DE and massive neutrinos [14–16].

In this work, we focus on the cross-correlations of the ISWRS with the CMB-lensing potential and the galaxy distribution. As the RS effect anti-correlates with both of them [17, 18], these cross-spectra are characterised by the presence of a sign inversion that occurs when passing from the linear (ISW) to the nonlinear (RS) regime. Moreover, the position of the sign inversion, which indicates the appearance of nonlinearities, shifts towards smaller cosmological scales due to the suppression of the matter power spectrum resulting from the presence of massive neutrinos [17, 18].

We develop an analytical method to produce the ISWRS spectra using the nonlinear modelling of the matter power spectrum implemented in the Boltzmann solver code `CAMB`¹ [19]. Given the large redshift extension investigated in this work, we consider only two of the revised `Halofit` [20] models implemented: the Takahashi2012 model [21], extended to massive neutrino cosmologies by including the Bird’s correction [22]; the Mead2020 model [23], which is an improvement over the Mead2016 model [24] concerning the treatment of Baryon Acoustic Oscillations (BAO) nonlinear damping. We then validate this analytical approach by comparing it with signals extracted from the “Dark Energy and Massive Neutrino Universe” (DEMNUi) N-body numerical simulations [18].

These studies are particularly relevant in light of ongoing and forthcoming galaxy surveys, such as Euclid [25–27] and SKA [28–34], and CMB surveys, such as CMB-S4 [35, 36], which aim to achieve measurements of small scales with high precision and accuracy, such that the possibility of detecting the RS effect could become concrete [37].

This paper is organised as follows. In Section 2 we recap the theoretical framework of the cross-correlations of the ISWRS signal with the CMB-lensing potential and the galaxy distribution in the presence of massive neutrinos. In Section 3 we present how we model ISWRS nonlinearities using measurements from the DEMNUi simulations. In Section 4 we test the analytical method for the cross-correlation between the ISWRS signal and the CMB-lensing potential against the DEMNUi simulated cross-spectrum. In Section 5 we validate the cross-correlation between the ISWRS signal and the galaxy distribution against the cross-spectrum measured from the DEMNUi mock maps. In Section 5 we evaluate the predictability of M_ν via the estimation of the sign inversion position and model the ISWRS-galaxy cross-spectrum for different redshift ranges. Finally, in Section 6 we draw our conclusions.

¹<https://CAMB.readthedocs.io/en/latest/>

2 The Integrated Sachs Wolfe and the Rees Sciama effects

When CMB photons pass through a time-varying gravitational potential well along their path from the last scattering surface to us, they undergo a variation in energy that translates into a variation in temperature known as the Integrated Sachs Wolfe effect:

$$\frac{\Delta T_{\text{ISW}}}{T_0}(\hat{\mathbf{n}}) = \frac{2}{c^2} \int_{t_{ls}}^{t_0} dt \dot{\Phi}(\hat{\mathbf{n}}, \chi, t), \quad (2.1)$$

where $\hat{\mathbf{n}}$ is a unit direction vector on the sphere, T_0 is today (t_0) CMB temperature, t_{ls} is the time at the last scattering surface, χ the comoving distance and $\dot{\Phi}$ is the time derivative of the gravitational potential. This effect is mainly due to the presence of DE that induces an accelerated background expansion of the Universe and counteracts the gravitational potential Φ inducing a not vanishing $\dot{\Phi}$ [15, 38]. The nonlinear growth of density perturbations produces additional temperature perturbations, leading to the RS effect. The RS contribution to temperature fluctuations is much more slow over time than the late ISW one, which means that at high redshifts RS predominates over the late ISW [39]. Consequently, we are able to observe $\dot{\Phi} \neq 0$ even when the DE effect becomes negligible. Moreover, the presence of massive neutrinos induces a not vanishing derivative of the gravitational potential even during matter domination era. This is because, after becoming non-relativistic, neutrinos free-stream with large thermal velocities that suppress the growth of neutrino density perturbations on scales smaller than the so-called “free-streaming length” [9, 16]:

$$\lambda_{\text{FS}}(z, m_\nu) \simeq 8.1 \frac{H_0(1+z)}{H(z)} \frac{1 \text{ eV}}{m_\nu} h^{-1} \text{Mpc}, \quad (2.2)$$

where m_ν is the mass of the single neutrino species (i.e. ν_e, ν_μ or ν_τ), $H(z)$ is the Hubble parameter as a function of the redshift z and $H_0 \equiv H(z=0)$ is the Hubble constant. Moreover, because of the gravitational back reaction effects, the evolution of cold dark matter (CDM) and baryon densities is affected as well by the presence of neutrinos, and the total matter power spectrum is suppressed at scales $\lambda \ll \lambda_{\text{FS}}$ [40]. Consequently, on small cosmological scales the free-streaming of neutrinos induces a slow decay of the gravitational potential, acting during both the matter and DE dominated eras, and this effect depends on the total neutrino mass $M_\nu = \sum m_\nu$. The more neutrinos are massive, the more the matter power spectrum will be suppressed with respect to the massless neutrino case, and therefore nonlinearities will appear on smaller scales.

One of the effects of massive neutrinos which has been poorly investigated so far is the shift they induce in the sign inversion that characterises the cross-power spectra between the ISWRS signal and the CMB-lensing potential ($P_{\dot{\Phi}\Phi}$), and between the ISWRS signal and the galaxy distribution ($P_{\dot{\Phi}\delta}$). These sign inversions appear because of the anti-correlation between the RS and both the CMB-lensing potential and the galaxy distribution, that depend on the gravitational potential Φ . While on large scales (i.e. the linear regime) the gravitational potential decays because of the Universe expansion ($\Phi < 0$, $\dot{\Phi} < 0$), on small scales (i.e. the nonlinear regime) Φ grows because of nonlinear structures formation ($\Phi < 0$, $\dot{\Phi} > 0$). Consequently, the time derivative of the gravitational potential associated to the ISWRS signal is negative in the linear regime and positive in the nonlinear one. The net result is that $\langle \Phi \dot{\Phi} \rangle > 0$ in the late ISW regime, producing a positive correlation, and $\langle \Phi \dot{\Phi} \rangle < 0$ in the RS regime, producing an anti-correlation [41].

Following the example of [17, 42, 43], we report below the dimensionless and scaled (i.e. divided by $3/2[H_0/(ck)]^2\Omega_m$) forms of $P_{\dot{\Phi}\Phi}$ and $P_{\dot{\Phi}\delta}$ in Limber approximation [16, 43]:

$$\Delta_{\dot{\Phi}\Phi}^2 = \frac{4\pi}{(2\pi)^3} \frac{k^3 P_{\dot{\Phi}\Phi}(k, z)}{[F(k)H(z)/ca(z)]}, \text{ with } P_{\dot{\Phi}\Phi}(k, z) = -\frac{1}{2} \frac{H(z)}{a(z)} [F(k)]^2 \left(\partial_z \frac{P_{\delta\delta}(k, z)}{a^2(z)} \right), \quad (2.3)$$

$$\Delta_{\dot{\Phi}\delta}^2 = \frac{4\pi}{(2\pi)^3} \frac{k^3 P_{\dot{\Phi}\delta}(k, z)}{[F(k)H(z)/ca(z)]}, \text{ with } P_{\dot{\Phi}\delta}(k, z) = \frac{1}{2} H(z) F(k) \left(\partial_z \frac{P_{\delta\delta}(k, z)}{a^2(z)} \right), \quad (2.4)$$

where $a(z)$ is the scale factor, $P_{\delta\delta}$ is the matter power spectrum, k is the wavenumber, and

$$F(k) = \frac{3\Omega_m H_0^2}{2c^2 k^2},$$

with Ω_m the matter density parameter and c the speed of light.

We compute each term of Equations (2.3) and (2.4) with CAMB and use both the nonlinear modellings chosen for the matter power spectrum (i.e. Takahashi2012 and Mead2020). The absolute values of the results are shown in Figure 1 and Figure 2, for both the Takahashi2012 and Mead2020 nonlinear modelling, at different redshift values, for the four total neutrino masses considered in this work.

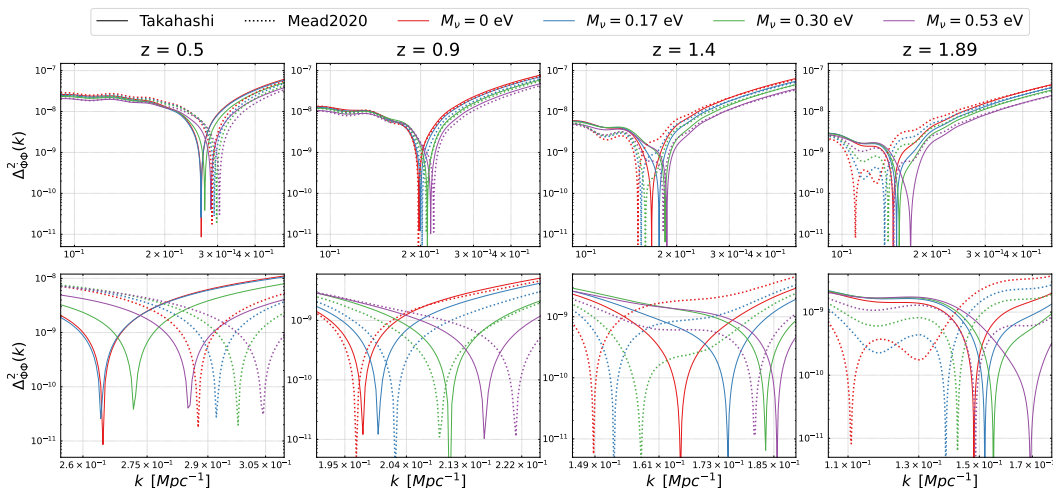


Figure 1: *Top:* Absolute values of the dimensionless and scaled form of the ISWRS–CMB–lensing potential cross-spectra as a function of the wavenumber k at $z = 0.5, 0.9, 1.4, 1.89$ for the four neutrino total masses considered ($M_\nu = 0, 0.17, 0.30, 0.53$ eV as red, blue, green and purple lines, respectively), obtained via the Takahashi2012 model (solid lines) and the Mead2020 model (dotted lines). *Bottom:* Zoom-in of the top panels on the sign inversion region.

The panels of both Figures 1-2 show how the presence of nonlinearities varies with time. As already mentioned, the more we travel back in time, the more the RS effect will dominate over the late ISW. Considering that at large redshifts the RS traces not only nonlinearities at small scales, but even the production of filamentary structures (visible at scales of few hundreds Mpc) [39], we see the shifts of the sign inversion towards smaller k (i.e. larger cosmological scales) from $z = 0.5$ to $z = 1.89$. In the bottom panels, the zoom in of the sign inversion region highlights the effect of massive neutrinos that we expected to find: the more

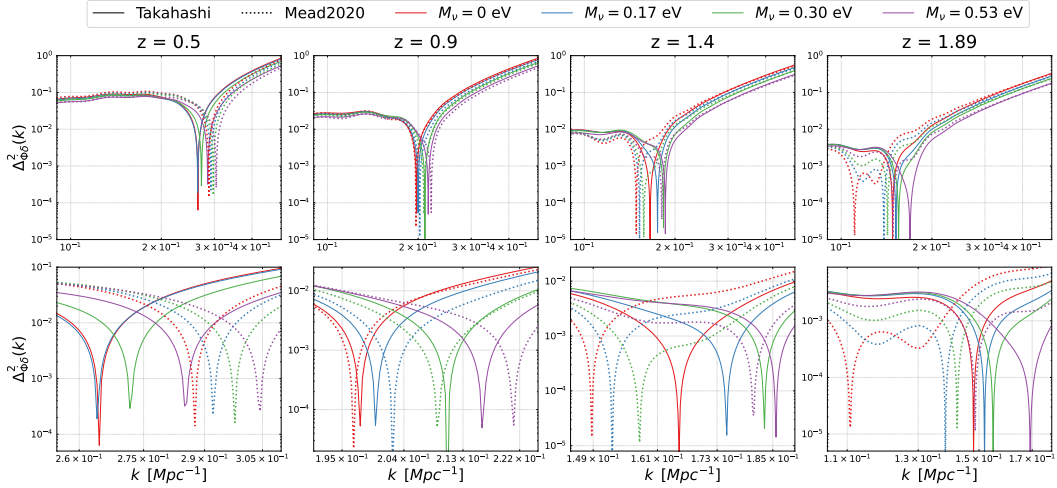


Figure 2: *Top:* Absolute values of the dimensionless and scaled form of the ISWRS–galaxy distribution cross-spectra as a function of the wavenumber k at $z = 0.5, 0.9, 1.4, 1.89$ for the four neutrino masses considered ($M_\nu = 0, 0.17, 0.30, 0.53$ eV as red, blue, green and purple lines, respectively), obtained via the Takahashi2012 model (solid lines) and the Mead2020 model (dotted lines). *Bottom:* Zoom-in of the top panels on the sign inversions region.

neutrinos are massive, the more nonlinearities (and therefore the sign inversion) appear on smaller cosmological scales. The only exception, for both $\Delta_{\Phi\Phi}^2$ and $\Delta_{\Phi\delta}^2$, is the trend obtained for $M_\nu = 0.17$ eV using the Takahashi2012 model at $z = 0.5$, where the power spectra show the sign inversion at scales slightly larger than the massless neutrino case. This effect is probably due to inaccuracies in the nonlinear modelling (see Appendix A for further details).

These results also highlight the different behaviour of the two models. At small redshifts the Takahashi2012 model predicts an higher level of nonlinearities than the Mead2020 model. Indeed, in the panels of Figures 1-2 corresponding to $z = 0.5$, the wavenumbers k where Takahashi2012 sign inversions occur are smaller than Mead2020 ones. However, in both Figures it is easy to notice that at $z = 0.9$ and $z = 1.4$ there is a switch of trend between Takahashi2012 and Mead2020, and at $z = 1.89$ the Mead2020 model predicts an higher level of nonlinearities with respect to Takahashi2012.

The presence of massive neutrinos is expected to affect similarly also the angular power-spectra of both these cross-correlations, that actually depend on the redshift derivative of the matter power spectrum $P_{\delta\delta}$, and can be computed via [44]:

$$C_\ell^{\Phi\Phi} = \frac{1}{2} \left(\frac{3\Omega_m H_0^2}{2c^2 k^2} \right)^2 \int_{z_{\min}}^{z_{\max}} dz \frac{\chi(z_{ls}) - \chi(z)}{\chi(z_{ls})\chi^3(z)} \left[\partial_z \frac{P_{\delta\delta}(k, z)}{a^2(z)} \right], \quad (2.5)$$

where $z_{ls} = 1100$, and [16, 37]:

$$C_\ell^{\Phi g} = \frac{3\Omega_m H_0^2}{2(\ell + 1/2)^2} \int_{z_{\min}}^{z_{\max}} dz n(z)b(z)H(z)a(z) \left[\partial_z \frac{P_{\delta\delta}(k, z)}{a^2(z)} \right], \quad (2.6)$$

where $n(z)$ and $b(z)$ are the galaxy selection function and the galaxy bias, respectively. The integral limits used in this work are: $z_{\min} = 0.02$ and $z_{\max} = 1.89$. This is because we use Equations (2.5) and (2.6) to compute the theoretical predictions that are compared against the cross-spectra measured from the DEMNUni maps, that cover the redshift range [0.02, 1.89]

(see Section 3). Apart from $n(z)$ and $b(z)$, all the ingredients of Equations (2.5) and (2.6) have been obtained via CAMB.

3 Nonlinear modelling with N-body simulations

The choice to investigate the nonlinear regime requires the use of large N-body simulations for validation tests. For this work, we use the ‘‘Dark Energy and Massive Neutrino Universe’’ (DEMNUi) [18] N-body cosmological simulations to model at small scales the ISWRS signal and their cross-correlations with the CMB-lensing and the galaxy distributions.

3.1 The Dark Energy and Massive Neutrino Universe simulations

The DEMNUi simulations have been produced with the aim of investigating large-scale structures in the presence of massive neutrinos and dynamical dark energy (DDE), and they were conceived for the nonlinear analysis and modelling of different probes, including dark matter, halo, and galaxy clustering [45–55], weak lensing, CMB-lensing, SZ and late ISW effects [18, 56–58], cosmic void statistics [59–63], and cross-correlations among these probes [64]. To this end, they combine a good mass resolution with a large volume to include perturbations both at large and small scales. In fact, these simulations follow the evolution of 2048^3 cold dark matter (CDM) and, when present, 2048^3 neutrino particles in a box of side $L = 2 h^{-1} \text{Gpc}$. The fundamental frequency of the comoving particle snapshot is, therefore, $k_F \approx 3 \times 10^{-3} h/\text{Mpc}$, while the chosen softening length is $20 \text{ kpc}/h$. The simulations are initialised at $z_{\text{ini}} = 99$ with Zel’dovich initial conditions. The initial power spectrum is rescaled to the initial redshift via the rescaling method developed in Ref. [65]. Initial conditions are then generated with a modified version of the N-GenIC software, assuming Rayleigh random amplitudes and uniform random phases. The DEMNUi simulations have been performed using the tree particle mesh-smoothed particle hydrodynamics (TreePM-SPH) code GADGET-3, an improved version of the code described in [66], specifically modified in [67] to account for the presence of massive neutrinos. This version of GADGET-3 follows the evolution of CDM and neutrino particles, treating them as two distinct collisionless fluids. Given the large amount of memory required by the simulations, baryon physics is not included. This choice, however, does not affect the results of this work [22]. The DEMNUi suite is composed by a total of sixteen simulations accounting for different combinations of the total neutrino mass M_ν and the DE EoS. In this project, we have worked with four of them, characterised by a baseline Planck 2013 cosmology [5], namely a flat ΛCDM model with $\tau = 0.0925$, $n_s = 0.96$ and $A_s = 2.13 \times 10^{-9}$, generalised to a $\nu\Lambda\text{CDM}$ by varying only the sum of the neutrino masses over the values $M_\nu = 0, 0.17, 0.30, 0.53 \text{ eV}$ (whence the corresponding values of Ω_ν and Ω_{cdm} , keeping fixed $\Omega_m = 0.32$ and $\Omega_b = 0.05$), considering a degenerate neutrino mass hierarchy. As aforementioned, in this work we use maps that cover a range of redshift that goes from $z_{\text{min}} = 0.02$ to $z_{\text{max}} = 1.89$. For each simulation, 63 outputs have been produced, logarithmically equispaced in the scale factor $a = 1/(1+z)$, in the redshift interval $z = 0 - 99$, 49 of which lay between $z = 0$ and $z = 10$. For each of the 63 output times, it has been produced on-the-fly one particle snapshot, composed of both CDM and neutrino particles, one 3D grid of the gravitational potential, Φ , and one 3D grid of its time derivative, $\dot{\Phi}$, with a mesh of dimension 4096^3 that covers a comoving volume of $(2 h^{-1} \text{Gpc})^3$. The map-making procedure has been developed taking into account the standard pixelisation approach introduced by the Hierarchical Equal-Area isoLatitude Pixelization [68] (HEALPix²).

²<http://healpix.sourceforge.net>

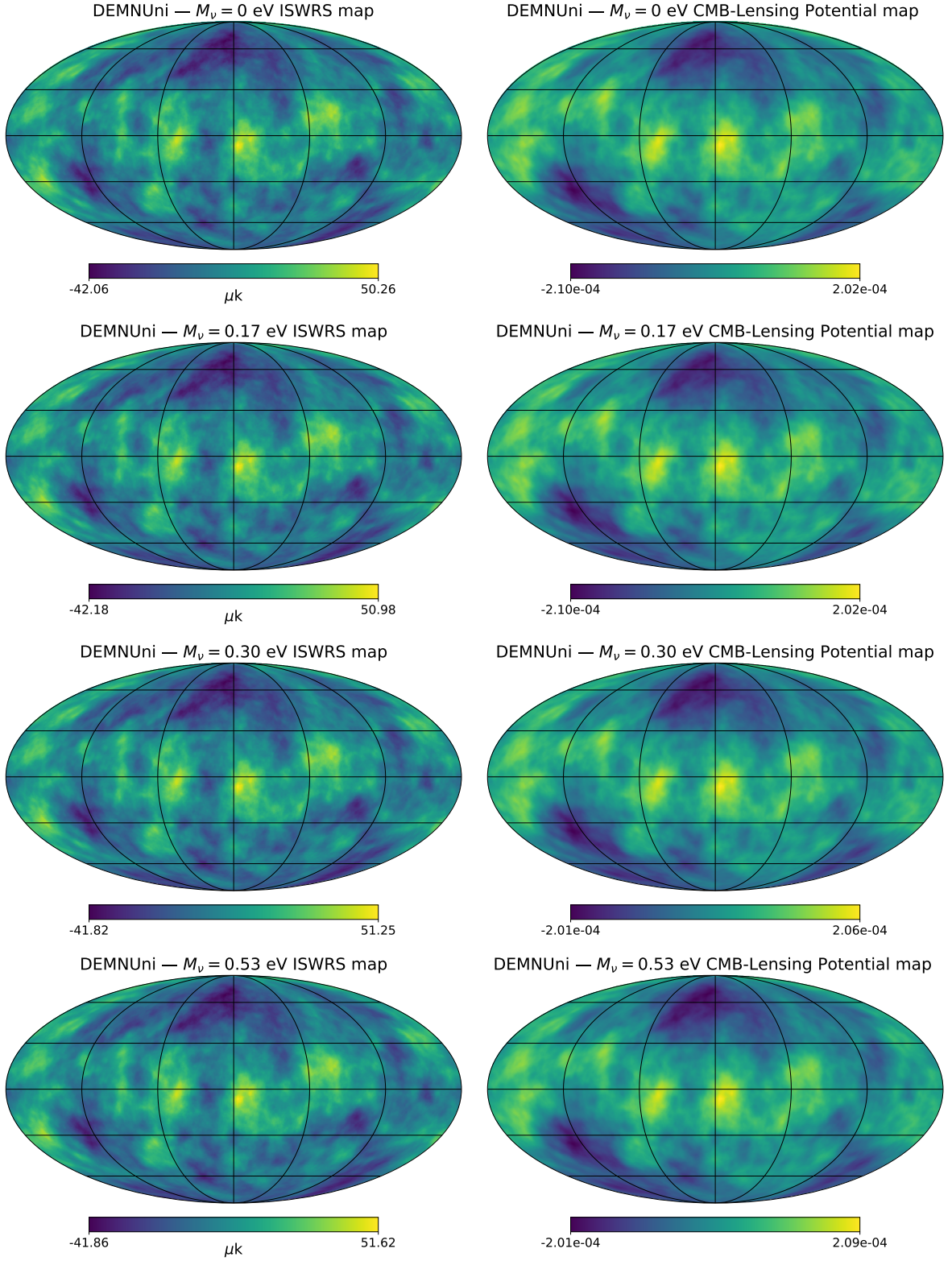


Figure 3: Full-sky maps of ISWRS (*left column*) and CMB-lensing potential (*right column*) obtained from the DEMNUi simulations for the four cosmologies used in this work: Λ CDM and $\nu\Lambda$ CDM with $M_\nu = 0.17, 0.30, 0.53$ eV (from top to bottom). These maps have a pixel number and resolution given by $N_{\text{side}} = 2048$ and a RING ordering, following the procedure described in Section 3.2.

3.2 Map-making procedure: ISWRS and CMB-lensing

The procedure followed to build ISWRS and CMB-lensing potential maps is an adaptation of the one developed in [69]. To make ISWRS maps (left column of Figure 3), CMB photons are ray-traced along the undeflected line of sight through the 3D field $\dot{\Phi}$. An analogous kind of ray-tracing has been applied to the 3D Φ -grids as well, in order to produce CMB-lensing potential maps (right column of Figure 3) from the same realisation of the Universe as for the ISWRS maps, and compute the cross-correlation between the two maps. Comparing the left and right columns of Figure 3, it is possible to appreciate at a glance how the two signals are highly correlated. Comparing the scales of each rows, the slight difference due to the different M_ν considered emerges. To this aim, the $\dot{\Phi}$ - and Φ -grids have been stacked around the observer, located at $z = 0$, and it has been applied the replication and randomisation procedure designed by [69]. This particular 3D tessellation scheme is required to avoid both the repetition of the same structures along the line of sight and the generation of artifacts like ripples in the simulated deflection-angle field, which can be avoided only if the peculiar gravitational potential is continuous transversely to each line of sight.

3.2.1 Simulated ISWRS and CMB-lensing auto-spectra

The power spectra extracted from the maps of Figure 3 are reported in Figure 4. For comparison, the orange squares and the orange dashed lines represent theoretical predictions in the linear regime obtained with **CAMB** for the massless neutrino case, in order to highlight the differences from the nonlinear modelling. The subpanels represent the percentage relative differences of the $\nu\Lambda$ CDM models with respect to the massless neutrino one. There is a good agreement between the simulated ISWRS signals and the ones predicted with **CAMB** for $\ell < 100$ (which roughly corresponds to the transition between the linear and the nonlinear regimes [70, 71]). Past the linear limit, **CAMB** predictions fail, given that the RS contribution is not implemented in the code. The CMB-lensing potential linear prediction for the massless neutrino case, similarly, perfectly agrees with DEMNUni mocks up to the linear limit and then shows a lack of power with respect to the nonlinear ones.

Focusing on spectra extracted from maps, it is easy to appreciate at small scales the differences produced in the ISWRS induced temperature anisotropies by free-streaming neutrinos with different total masses. Similar effects are noticeable also in the lensing potential power spectra, considering the percentage relative differences with respect to the massless neutrino case (see subpanels of Figure 4). In particular, as expected, the effect of massive neutrinos produces a suppression of power in the CMB-lensing potential which increases with the neutrino mass and decreases with the angular scale (at low ℓ). These effects are reasonably due to the nonlinear excess of suppression of the total matter power spectra with respect to linear expectations in the presence of massive neutrinos, that counteract the nonlinear evolution [18].

3.3 Map-making procedure: projected galaxy mocks

The procedure followed to construct galaxy maps is an adaptation of the one developed in [57, 72] for convergence maps. The convergence maps are extracted with a postprocessing procedure acting on the N-body particle snapshots to create matter particle full-sky lightcones [73, 74]. The standard way to build lightcones is to pile up high-resolution boxes within concentric cells to fill the lightcone to the maximum desired source redshift. With the observer placed at $z = 0$, the volume of the lightcone is sliced into full-sky spherical shells of

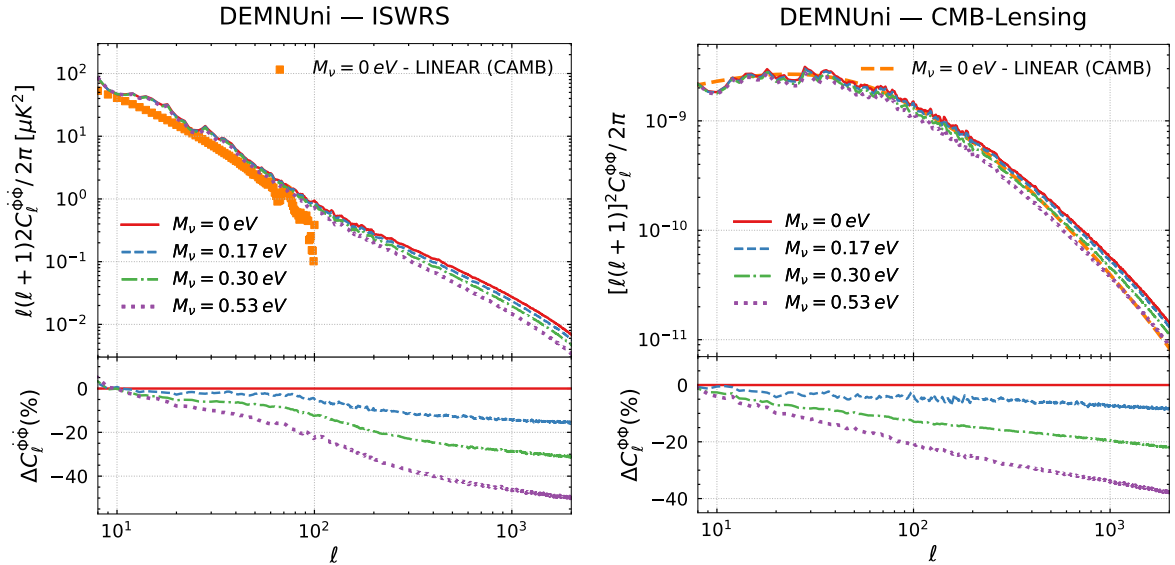


Figure 4: *Left:* Angular power spectra of the total ISWRS induced temperature anisotropies computed from DEMNUUni maps with $M_\nu = 0, 0.17, 0.30, 0.53 \text{ eV}$ (solid red, dashed blue, dot-dashed green, dotted purple lines, respectively) compared with linear prediction (orange squares). *Right:* Same for angular power spectra of the CMB-lensing. In both subpanels, the percentage relative differences with respect to the massless neutrino case is reported.

the desired thickness in redshift. All the particles distributed within each of these 3D matter shells are then projected onto 2D spherical maps, assigning a specific sky pixel to each particle, via HEALPix pixelisation procedure. Then integration along the undeflected line-of-sight is applied to obtain the convergence maps accounting for the lensing efficiency in the desired redshift range. A very similar method has been applied to the DEMNUUni galaxies to construct projected galaxies mocks [51] (see Figure 5). Specifically, in order to reproduce the galaxy distribution in the DEMNUUni simulations, the SubHalo Abundance Matching (SHAM) technique [55] has been used. The SHAM method assumes a one-to-one relation between a physical property of a dark matter halo/subhalo and an observational property of the galaxy that it hosts. In particular, it assumes that the most massive galaxies form in the dark matter haloes characterised by the deepest potential wells. Galaxies are linked to the corresponding dark matter structures using stellar mass or luminosity as galaxy property and a measure of halo mass or the circular velocity, as halo property (i.e. a proxy of the depth of the local potential well). Here we link the stellar mass to the halo mass using the Moster et al. (2010) [75] parameterised stellar-to-halo mass relation, fitted against the DEMNUUni simulations. As the SHAM galaxy catalogues are fitted against observations, they guarantee an high-degree of agreement with real data from galaxy surveys [76, 77].

Applying to the SHAM galaxy catalogues the same stacking technique as for particle co-moving snapshots, we have generated full-sky mock galaxy catalogues from the DEMNUUni simulations in different cosmological models.

3.3.1 Galaxy bias and selection function from DEMNUUni simulations

The galaxy bias and selection function necessary to compute the analytical predictions of the cross-spectra between ISWRS and galaxies (see Equation (2.6)) have been directly extracted

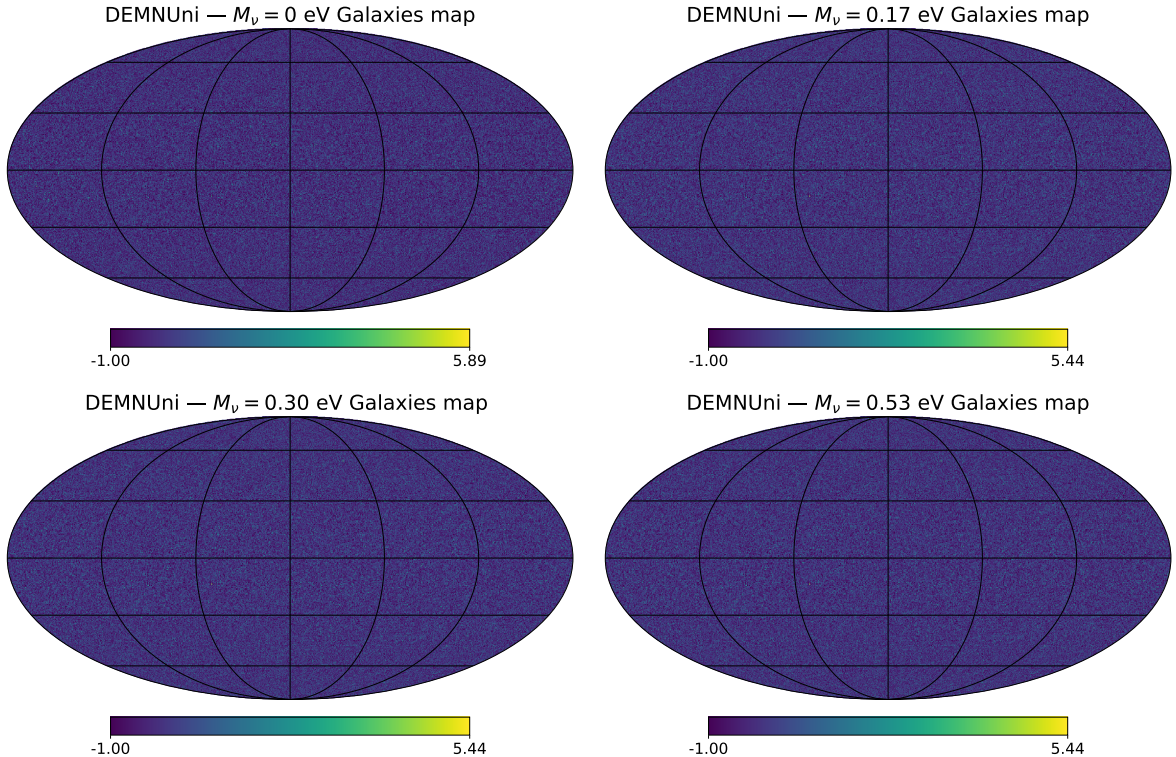


Figure 5: Full-sky galaxies maps obtained for the four cosmologies used in this work: Λ CDM and $\nu\Lambda$ CDM with $M_\nu = 0.17, 0.30, 0.53$ eV. These maps have a pixel number and resolution given by $N_{\text{side}} = 2048$ and a RING ordering, following the procedure described in Section 3.3.

from the DEMNUni simulations. This guarantees a more accurate comparison between mocks and analytical predictions.

Galaxy selection function The galaxy selection function extracted from DEMNUni Λ CDM map can be modelled via the following equation:

$$n_{\text{DEMNUni}}(z) = A \left(\frac{z}{z_0} \right)^B \exp \left[- \left(\frac{z}{z_0} \right)^C \right], \quad (3.1)$$

where $A = 1.89$, $B = 1.95$, $C = 1.41$ and $z_0 = 0.88$.

This is the $n(z)$ used to compute all the theoretical predictions to be compared with DEMNUni data, also for massive neutrino cases. This is because galaxy counts vary mostly because of the variation of the simulated cosmological volume, which depends on $H(z)$ via Ω_m - that has been fixed to 0.32 for all the simulations (and consequently for all the theoretical predictions) - and via the DE EoS, whose presence has not been taken into account in this work. As a result, the normalised galaxy counts do not undergo any significant change due to the variation of M_ν , and consequently it is possible to exploit the same $n(z)$ to compute all the theoretical predictions. We have verified this measuring the galaxy counts from the DEMNUni catalogues with different values of M_ν , obtained via the SHAM technique applied to COSMOS2020 and SDSS observations [55].

In Figure 6, together with DEMNUni $n(z)$, we show the galaxy selection function expected

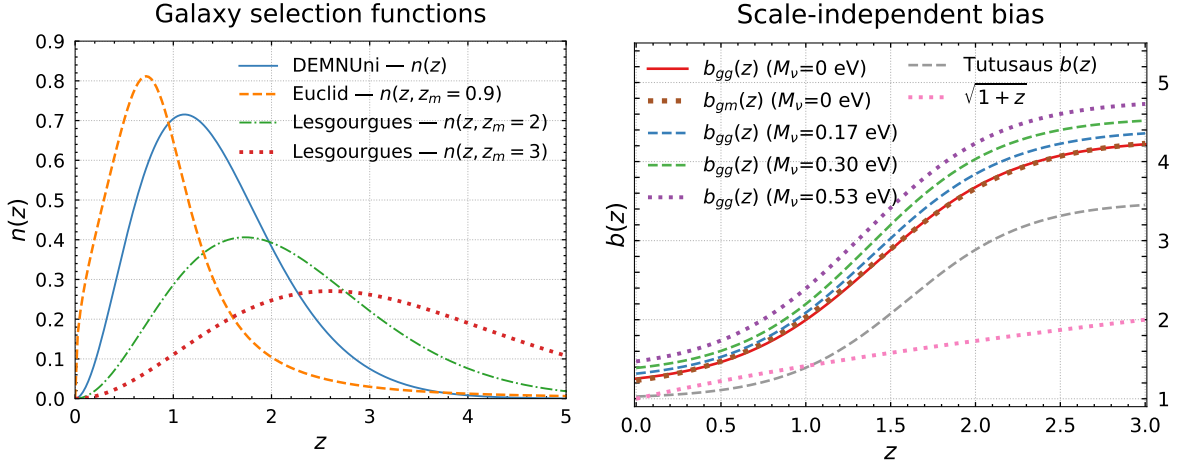


Figure 6: *Left:* Galaxy selection functions: the solid blue line is extracted from DEMNUni data; the dashed orange line is the one assumed for the photometric Euclid survey; the dot-dashed green and the dotted red lines are taken from Lesgourgues et al. (2008) [16] with $z_m = 2, 3$ respectively. *Right:* Scale-independent galaxy bias: the solid red, dashed blue, dot-dashed green and dotted purple lines are the $b_{gg}(z)$ extracted from the DEMNUni simulations for $M_\nu = 0, 0.17, 0.30, 0.53$ eV, respectively; the dotted brown line is the $b_{gm}(z)$ extracted from the DEMNUni simulations for the massless neutrino case only; the dashed grey line is the Tutusaus bias and the dotted pink line is the $\sqrt{1+z}$ bias.

for the photometric Euclid survey [25, 26]:

$$n_{\text{Euclid}}(z) = \frac{3 \cdot (z/z_0)^\alpha}{2 \cdot z_0} \exp\left[-\left(\frac{z}{z_0}\right)^\beta\right], \quad (3.2)$$

where $\alpha = 2$, $\beta = 1.5$, $z_0 = z_m/\sqrt{2}$, $z_m = 0.9$, and its extensions to a larger redshift range setting $z_m = 2, 3$ [16]. These functions have been used here to produce forecasts for future galaxy surveys, whose aim is to reach $z \geq 2$.

Scale-independent bias The galaxy scale-independent bias has been obtained for each cosmology from the square root of the ratio between the galaxy power spectrum, $P_{gg}(k, z)$, and the matter power spectrum, $P_{mm}(k, z)$, measured from DEMNUni comoving snapshots:

$$b_{gg}(z) = \left\langle \sqrt{\frac{P_{gg}(k, z)}{P_{mm}(k, z)}}} \right\rangle_k, \quad (3.3)$$

where the mean has been computed for large linear scales in the range $0.05 < k < 0.12$ in unit of Mpc^{-1} . Differently from the galaxy selection function, the neutrino mass affects the bias. The b_{gg} functions for $M_\nu = 0, 0.17, 0.30, 0.53$ eV shown in the right panel of Figure 6 have been fitted with:

$$b(z) = A + \frac{B}{1 + \exp[-(z - D)C]}, \quad (3.4)$$

where $A = 1.0$, $B = 2.5$, $C = 2.8$, $D = 1.6$. This is the bias currently assumed for the Euclid Flagship simulation, reported in [78]. From now on, we will refer to Equation (3.4) as the Tutusaus bias.

For the massless neutrino case alone, also the bias obtained from the square root of the ratio between the cross power spectrum between galaxy and matter has been computed:

$$b_{gm}(z) = \left\langle \sqrt{\frac{P_{gm}(k, z)}{P_{mm}(k, z)}}} \right\rangle_k, \quad (3.5)$$

(where the mean is again over large linear scales in the range $0.05 < k < 0.12$ in unit of Mpc^{-1}) and it is shown in Figure 6 after the fit with Tutusaus bias. Since it is affected by a lower level of shot noise, $b_{gm}(z)$ should allow us to describe better the connection between matter and galaxies, and consequently to improve the cross-correlation reconstruction. However, the results obtained do not differ significantly from those obtained using $b_{gg}(z)$, as we will show in Section 5.1.2. Finally, we show also the $\sqrt{1+z}$ bias, used in [26].

Scale-dependent bias A fit of scale-dependent bias has been computed from DEMNUni massless neutrino mocks as [79]:

$$b(k, z) = b_0(z) + b_1(z)k + b_2(z)k^2, \quad (3.6)$$

where b_0 is the scale-independent bias, b_2 is a correction due to peaks theory and b_1 is physically meaningless, but necessary to improve the fit. These parameters have been obtained via the fit of $P_{gg}(k, z)$ up to $k = 1 \text{ Mpc}^{-1}$. In Figure 7, we show the evolution of the b_i parameters on the left, while on the right we show the variation of the $b(k, z)$ at some chosen wavenumbers in the range of scales used to measure the scale-averaged the $b_{gg}(z)$ ($0.05 < k < 0.12$ in unit of Mpc^{-1}).

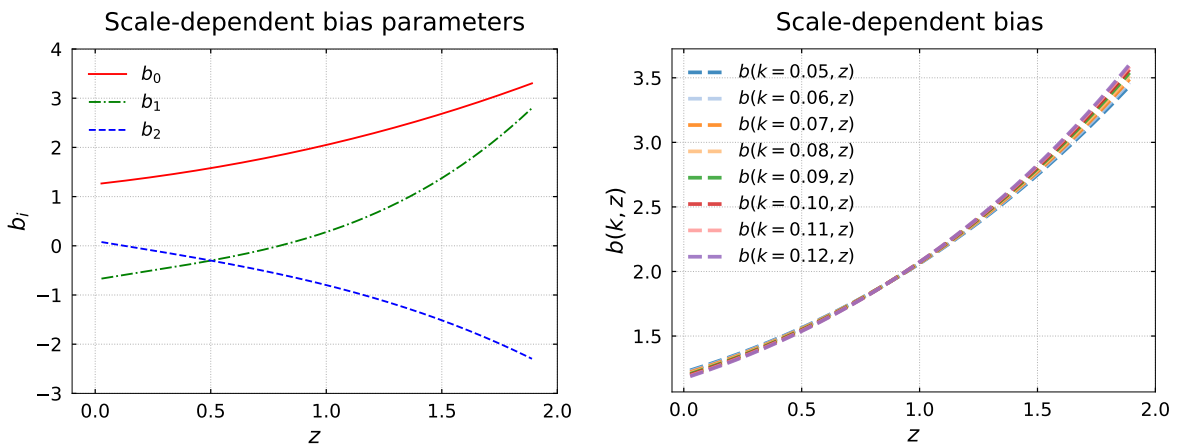


Figure 7: *Left:* Evolution of $b_i(z)$ parameters from Equation (3.6) in the DEMNUni maps redshift range $0.02 \leq z \leq 1.89$. *Right:* Scale-dependent bias computed for large scales in the range $0.05 < k < 0.12$.

3.3.2 Simulated projected galaxy auto-spectra

In Figure 8, we report the spectra extracted from the galaxy maps of Figure 5 after subtracting the shot-noise value.

In addition to the DEMNUni maps spectra, we report the theoretical predictions of the C_ℓ^{gg} computed in both the linear and nonlinear regimes, for the massless neutrino case, via [80]:

$$C_\ell^{gg} = \int_{z_{\min}}^{z_{\max}} dz \frac{H(z)}{c\chi^2(z)} [W^g(z)]^2 P_{\delta\delta}(k, z), \quad (3.7)$$

where:

$$W^g(z) = n(z) \cdot b(z), \quad (3.8)$$

and for $n(z)$ and $b(z)$ we use Equation (3.1) and Equation (3.3), respectively.

Both linear and nonlinear predictions do not perfectly agree with simulated spectra on large scales. This is due to the limited dimension of the simulation box, which does not allow to represent those scales. Conversely, on small scales there is a good agreement with the nonlinear prediction and the expected disagreement with the linear one.

Despite the presence of shot-noise in DEMNUni maps, its effect is negligible when cross-correlating these maps with ISWRS maps (since the noises of the two fields do not correlate). Furthermore, this analysis does not aim to reveal a perfect match between the simulations and the analytical predictions also because inaccuracies in the adopted nonlinear modelling.

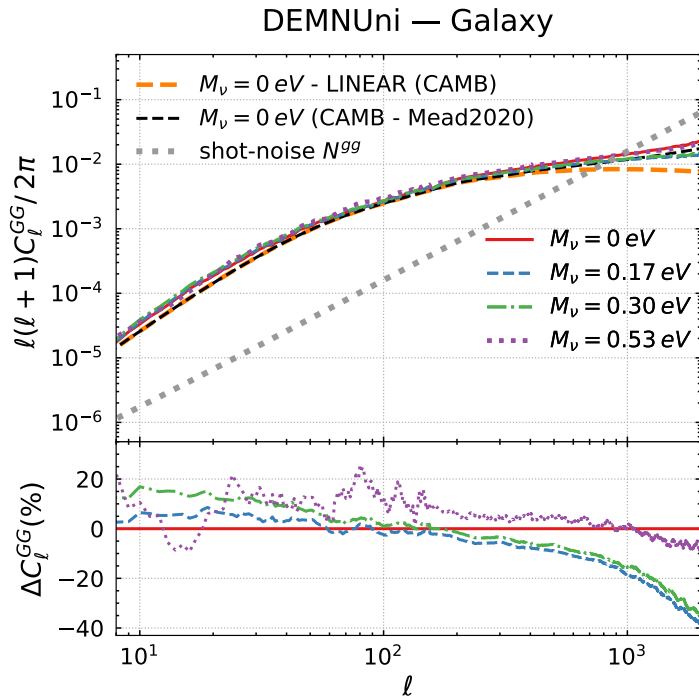


Figure 8: Galaxy angular auto-spectra extracted from DEMNUni maps for $M_\nu = 0, 0.17, 0.30, 0.53$ eV (solid red, dashed blue, dot-dashed green, dotted purple lines, respectively) with shot-noise (dotted grey line) subtracted, compared with theoretical predictions in the linear (dashed orange line) and Mead2020 nonlinear (dashed black line) regimes. In the subpanel, the percentage relative difference with respect to the massless neutrino case is reported.

The subpanel in Figure 8 represents the percentage relative differences of the $\nu\Lambda$ CDM models with respect to the massless neutrino one. Here the larger M_ν is, the smaller the dif-

ference with respect to the massless neutrino case is. This is because the matter perturbation suppression due to more massive neutrinos is compensated by a stronger clustering [81].

4 The ISWRS cross-correlation with the CMB-lensing potential

The presence of the sign inversion at large multipoles and its shift due to the variation of M_ν in the cross-power spectrum between the ISWRS effect and the CMB-lensing was already verified in [18], where they use DEMNUni maps obtained via ray-tracing from $z_{\min} = 0.02$ to $z_{\max} = 20.88$. Here, we verify the presence of the same effects in the cross-spectra of DEMNUni maps obtained up to $z_{\max} = 1.89$ and use these results to validate the analytical predictions computed using Equation (2.5).

The cross-correlations of the DEMNUni ISWRS and CMB-lensing potential maps for the four neutrino masses are shown in Figure 9, compared with the theoretical nonlinear prediction computed for the Takahashi2012 (left panels) and the Mead2020 (right panels) models. For completeness, also the theoretical cross-correlation predictions for the massless neutrino case in the linear regime have been reported.

The agreement between the simulation data and both the theoretical predictions obtained with CAMB up to $\ell \sim 100$ is quite impressive. Once exceeded $\ell \sim 100$, the anti-correlation between the RS effect and the CMB-lensing potential takes over, resulting in the characteristic sign inversion that appears in both simulations (as already shown in [18]) and nonlinear predictions. Moreover, both of them validate the expected result, because the more neutrinos are massive, the more they counteract nonlinear evolution (i.e. structure formation) and nonlinear effects appear at smaller cosmological scales. In other words, the more neutrinos are massive, the more the sign inversion shifts towards larger multipoles.

Focusing on the sign inversion position (subpanels), on the one hand the analytical predictions computed with the Mead2020 model show the sign inversions at smaller multipoles with respect to mocks and with respect to the Takahashi2012 model. On the other hand, the Takahashi2012 model almost perfectly reproduces the results of DEMNUni mocks for $M_\nu = 0.17, 0.30$ eV, while overestimating the ℓ correspondent to the sign inversion in the massless neutrino case and underestimating it in the more massive case. The differences between the two nonlinear models are strictly due to how nonlinearities are implemented in the two codes [21, 23, 51]. The achieved results disprove the counter-intuitive effect reported in [82], where for larger M_ν values the sign inversion position moves towards smaller multipoles.

5 The ISWRS cross-correlation with galaxies

The cross-spectra between the ISWRS signal and the galaxy distribution is the most used tool to investigate the ISWRS, because of its largest signal-to-noise ratio with respect to the spectra analysed in the previous Section. It is then the main focus of this work, which consists of verifying the presence of the sign inversion due to the anti-correlation between the RS effect and the galaxy distribution in the cross-correlation angular power spectra, showing that the position of this sign inversion depends on M_ν , as in the case of the cross-correlation between the ISWRS signal and the CMB-lensing potential [18]. The validation of these results via DEMNUni maps represents an improvement with respect to previous works: on the one hand, [16] computed this cross-correlation signal in massless and massive neutrino models, focusing only on the effects that neutrinos have in the linear regime; on the other hand, in

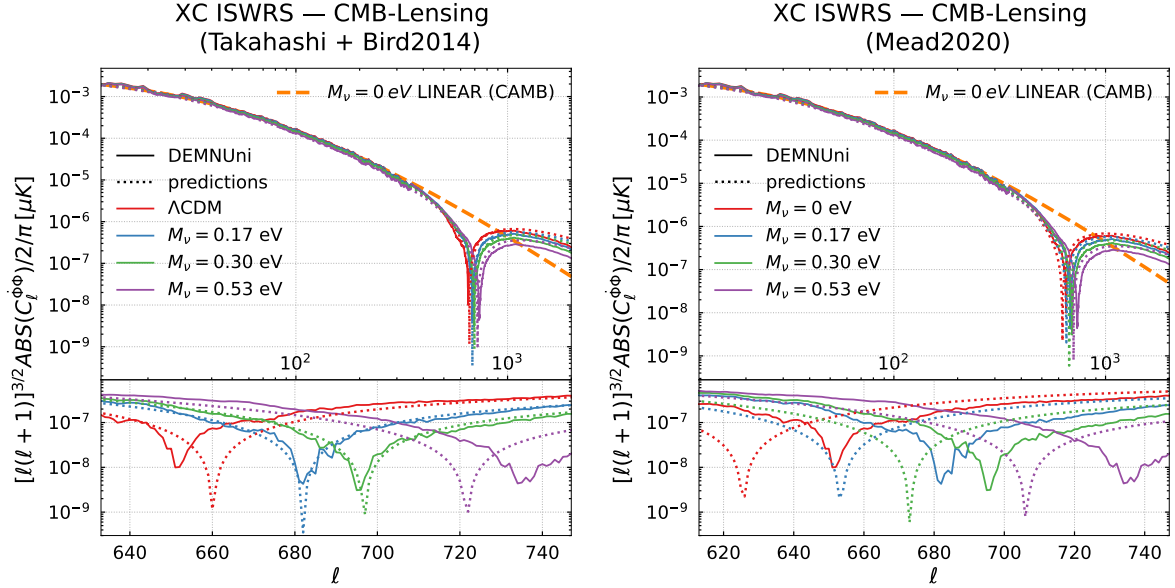


Figure 9: ISWRS – CMB-lensing angular cross-spectra for $M_\nu = 0, 0.17, 0.30, 0.53$ eV (solid red, blue, green and purple lines, respectively) from the DEMNUni maps compared to the theoretical predictions in the linear (dashed orange line) and nonlinear (dotted lines) regimes, obtained using the Takahashi2012 model (left) and the Mead2020 model (right), respectively. The subpanels show a zoom-in of the top panels on the sign inversions region.

the nonlinear regime, [43] focused only on the massless neutrino case, finding in the cross-spectrum the sign inversion due to the anti-correlation between the RS effect and the galaxy distribution.

The cross-correlations of the DEMNUni ISWRS and the galaxy distribution maps for the four neutrino masses are shown in Figure 10, compared with the theoretical nonlinear predictions, computed with Equation (2.6). For completeness, also the theoretical predictions for the massless neutrino case in the linear regime have been reported. All the theoretical predictions have been computed using $n(z)$ given by Equation (3.1) and the $b_{gg}(z)$ of Equation (3.3) associated with the cosmology analysed.

The results shown prove that also in the cross-correlation spectrum between the ISWRS and the galaxy distribution there is a sign inversion due to the anti-correlation between the two signals on small scales and that the position of the sign inversion is strongly affected by the presence of massive neutrinos. Also in this case, because of the suppression that massive neutrinos induce in the matter power spectrum, the larger M_ν is, the more nonlinearities appear on smaller scales and consequently the sign inversion position is shifted towards larger multipoles.

Moreover, the comparison of the simulated spectra with the theoretical predictions for both linear and nonlinear regimes is again quite impressive at large cosmological scales, while once passed $\ell \simeq 100$ nonlinear spectra dramatically differ from the linear one, because of the presence of the sign inversion. This result validates again the analytical method against mocks and makes it an extremely powerful tool to predict cross-spectra of future surveys in both linear and nonlinear regimes.

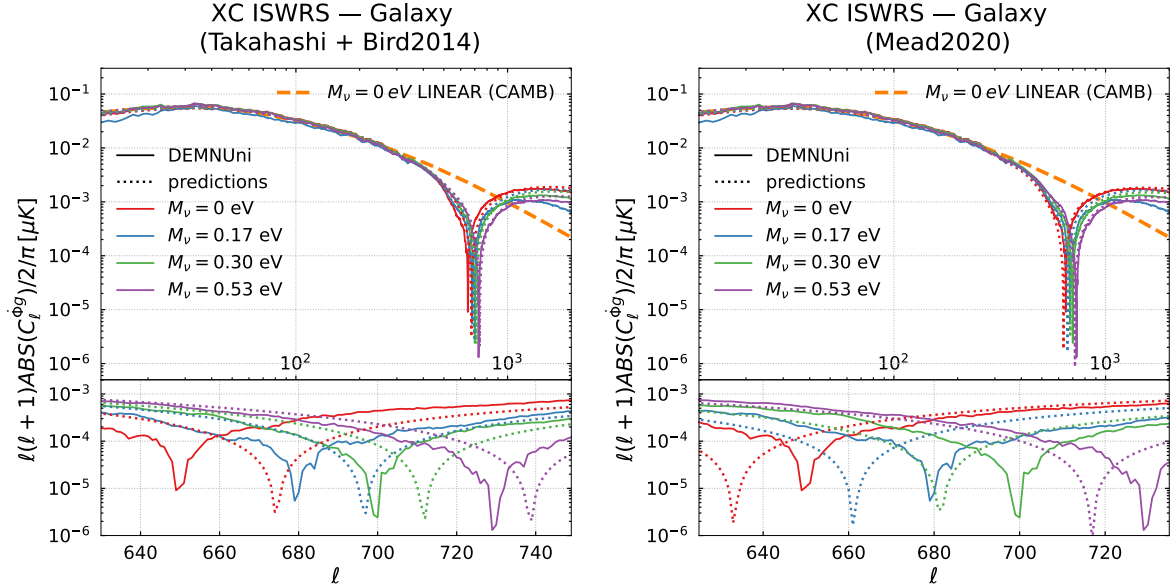


Figure 10: ISWRS-galaxy cross-spectra for $M_\nu = 0, 0.17, 0.30, 0.53$ eV (solid red, blue, green and purple lines, respectively) compared with theoretical predictions in the linear (dashed orange line) and nonlinear (dotted lines) regimes, obtained using the Takahashi2012 model (left) and the Mead2020 model (right), respectively. The subpanels show a zoom-in of the top panels on the sign inversions region.

Focusing on the sign inversion position (subpanels), the Takahashi2012 model shows inversions at larger multipoles with respect to DEMNUni spectra, and Mead2020 at smaller ones.

5.1 Nonlinear ISWRS-galaxy cross-spectra: effects of different bias modellings

As already mentioned, differently from the galaxy selection function, the bias strongly depends on the neutrino mass. We perform several tests to evaluate how the usage of different bias functions affects the comparison between predictions and DEMNUni simulations. Firstly, we produce theoretical predictions for the massive neutrino cases using both the corresponding bias and the massless neutrino bias functions and we verify that the more neutrinos are massive, the more the massless neutrino case bias fails in predicting the spectra (further details in Section 5.1.1). Secondly, we check, for the massless neutrino case alone, that using a scale-dependent bias function improves the agreement between theoretical predictions and simulations, as already verified in [43] (further details in Section 5.1.2). The results of these tests are shown in Figure 11 and Figure 12, respectively.

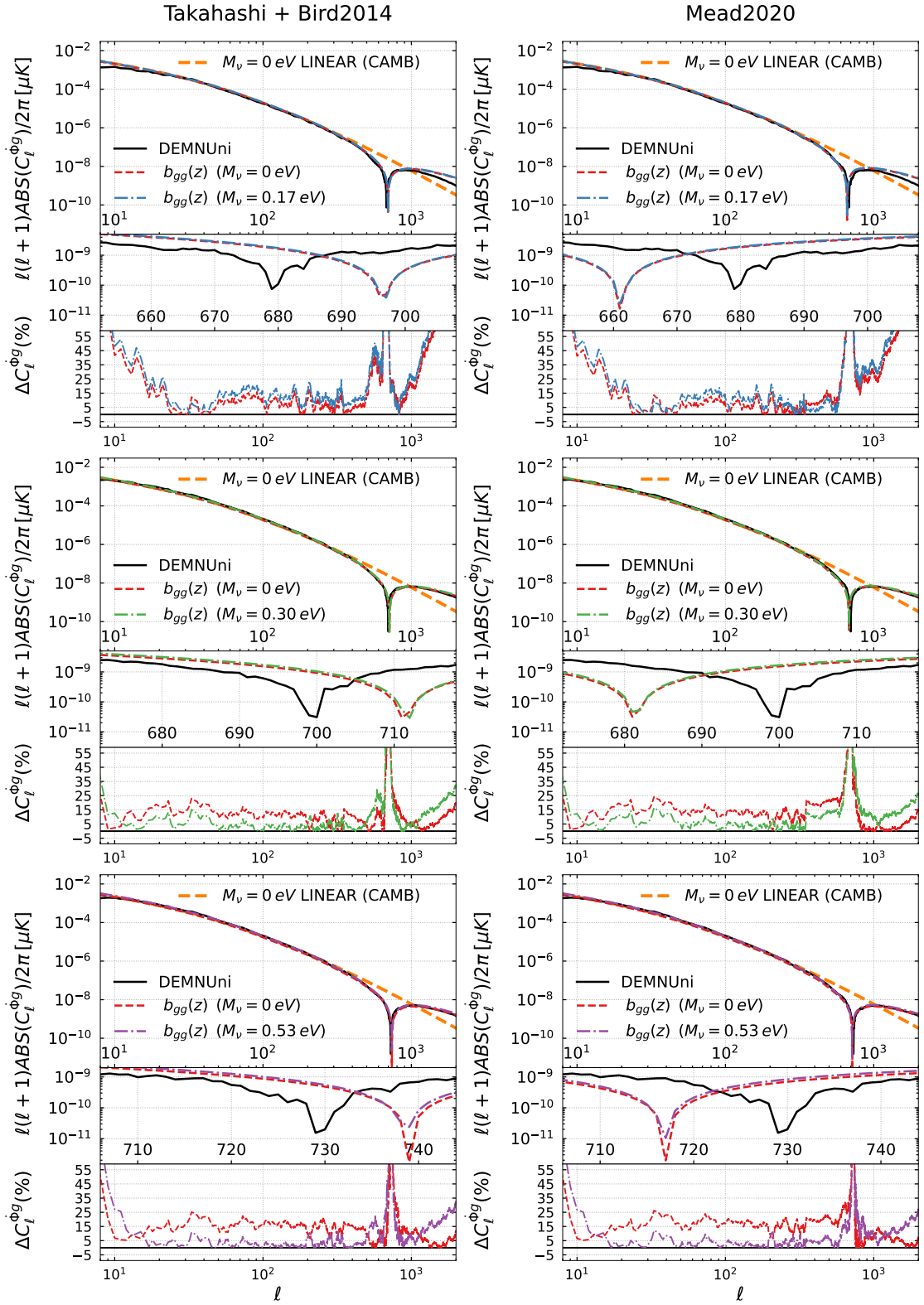


Figure 11: *Left:* Comparison between the simulated ISWRS-galaxy cross-correlations for $M_\nu = 0.17, 0.30, 0.53$ eV (solid black line) and theoretical predictions in the linear (dashed orange line) and nonlinear regimes, using the Takahashi2012 model combined with DEMNUni measurements of b_{gg} in the massless neutrino (dashed red) and massive neutrino cases for $M_\nu = 0.17$ eV (*top*, dot-dashed blue), $M_\nu = 0.30$ eV (*middle*, dot-dashed green) and $M_\nu = 0.53$ eV (*bottom*, dot-dashed purple), respectively. The middle subpanel of each plot shows a zoom-in of the sign inversion region, while the bottom one shows the absolute value of the percentage relative differences of the predictions with respect to the simulated measurements. *Right:* Same as the left panel for the Mead2020 model.

5.1.1 Massive neutrino impact on the scale-independent bias

First, we test how the analytical predictions for massive neutrino cosmologies vary with respect to mock data when using the bias fitted against the simulations for the $M_\nu > 0$ eV case and the bias of the massless neutrino case.

In Figure 11, the simulated cross-correlations are compared with linear predictions and with nonlinear predictions computed with both the massless neutrino galaxy bias and the galaxy bias associated with the specific neutrino model. The results for $\ell \leq 10$ can be neglected because of the inaccuracies of mocks on those scales.

For the $M_\nu = 0.17$ eV case, reported in top panels of Figure 11, the slight difference with respect to the other cases (and to the predictions), noticeable in the simulation data for very small and very large multipoles, induces a difference $> 35\%$ for $\ell < 30$ and $\ell > 1000$. Before the sign inversion range, the differences do not overcome 25% for the $M_\nu = 0.17$ eV bias and 15% for the massless neutrino case bias, for the Takahashi2012 modelling. In the case of the Mead2020 modelling, the difference is slightly smaller with the massive cosmology bias ($< 20\%$). The differences in the sign inversion positions consist of $\Delta\ell_{\text{DEMNU}_{\text{ni}}-\text{Takahashi2012}} \sim -18$ and $\Delta\ell_{\text{DEMNU}_{\text{ni}}-\text{Mead}} \sim +18$. Both nonlinear modellings show a difference between the predictions obtained with the two bias recipes at a level of $\sim 5\%$ and the sign inversions occur at the same multipole in the Mead2020 model, while there is a $\Delta\ell = 1$ for the Takahashi2012 one. The fact that the massless neutrino cosmology bias in the theoretical predictions leads to smaller differences with respect to the DEMNU_{ni} spectra can be explained considering the inaccuracies of the Takahashi2012 and Mead2020 models in reproducing the $M_\nu = 0.17$ eV case, as already shown in Section 2 (see Appendix A for further details).

In the $M_\nu = 0.30$ eV case, shown in centre panels of Figure 11, both nonlinear predictions, obtained with the Mead2020 and Takahashi2012 models, differ from the simulated data by no more than 15% in the $M_\nu = 30$ eV bias case and no more than 25% in the massless neutrino case. The differences in the sign inversion positions consist of $\Delta\ell_{\text{DEMNU}_{\text{ni}}-\text{Takahashi2012}} \sim -10$ and $\Delta\ell_{\text{DEMNU}_{\text{ni}}-\text{Mead}} \sim +20$. The difference between the two is larger than the previous case ($\lesssim 10\%$) and the sign inversions occur at the same multipole in the Mead2020 model, while there is a $\Delta\ell = 1$ for the Takahashi2012 one.

Conversely to the previous cases, in the $M_\nu = 0.53$ eV one, shown in bottom panels of Figure 11, the difference between the predictions is definitely more significant ($\sim 20\%$). The difference with respect to DEMNU_{ni} data is $\sim 10\%$ in the $M_\nu = 0.53$ eV bias case and no more than 25% in the massless neutrino case. The differences in the sign inversion positions consist of $\Delta\ell_{\text{DEMNU}_{\text{ni}}-\text{Takahashi2012}} \sim -10$ and $\Delta\ell_{\text{DEMNU}_{\text{ni}}-\text{Mead}} \sim +10$. Conversely to previous cases, here the sign inversions occur in the same multipole when using both Halofit models.

5.1.2 Scale-independent and scale-dependent bias effects in the neutrino massless neutrino case

For the massless neutrino case, both the $b_{mg}(z)$ and the $b(k, z)$ bias functions have been calibrated against the DEMNU_{ni} simulations. In Figure 12 we compare the effects of $b_{mg}(z)$, $b(k, z)$ and $b_{gg}(z)$ in the modelling of the theoretical nonlinear predictions. In agreement with the work of [43], we find that the amplitude of the predictions obtained with $b(k, z)$ better reproduces the simulated signals, with a percentage relative difference of $\sim 10\%$, lower than that obtained with $b_{gg}(z)$ and $b_{mg}(z)$. This is true up to $\ell = 200$, while for smaller scales the trend is inverted.

With regard to the sign inversion position, in the theoretical spectra it occurs at the same multipole for all bias recipes with both Takahashi2012 and Mead2020 model. The differences

with respect to the sign inversion in the simulated signals is $\Delta\ell_{\text{DEMNUni-Takahashi2012}} \sim -20$ and $\Delta\ell_{\text{DEMNUni-Mead}} \sim +20$.

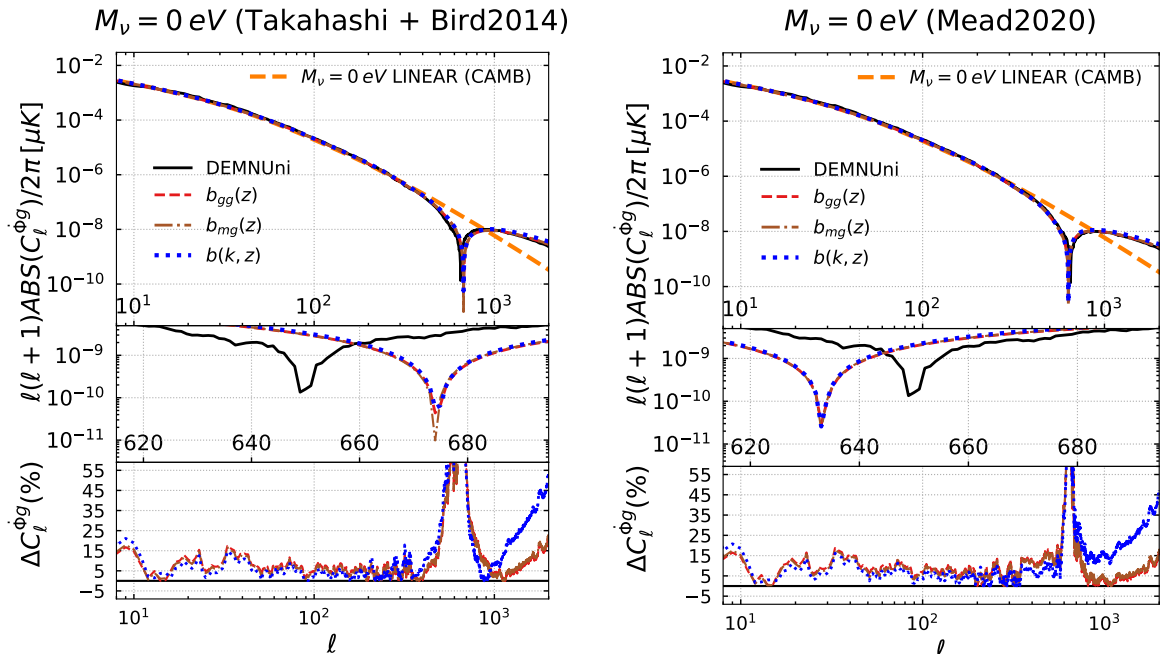


Figure 12: *Left:* Comparison between the simulated ISWRS-galaxy cross-correlation for $M_\nu = 0$ eV (solid black line) with theoretical predictions in the linear regime (dashed orange line) and nonlinear regime using the Takahashi2012 model. Three different DEMNUni galaxy bias models have been tested: the scale-independent DEMNUni $- b_{gg}$ bias (dashed red), the scale-independent DEMNUni $- b_{mg}$ bias (dot-dashed brown) and the scale-dependent DEMNUni $b(k, z)$ bias (dotted blue). The middle subpanel of the plot shows a zoom in of the sign inversion region, while the bottom one shows the absolute value of the percentage relative differences of the predictions with respect to the simulations. *Right:* Same as left, but with the Mead2020 model.

5.2 Nonlinear ISWRS-galaxy cross-spectra: detecting the neutrino mass

The results shown in the previous sections demonstrate the validity of the analytical method against DEMNUni simulations and that both mocks and predictions confirm what we expect from theory: more massive neutrinos induce a larger suppression in the matter power spectrum and shift the appearance of nonlinearities on smaller cosmological scales. Moreover, Figures 9 and 10 highlight the strict connection between the sign inversion position, ℓ_{inv} , and M_ν . In light of this, we decide to test if the detection of ℓ_{inv} in the cross-power spectrum between the ISWRS and the galaxy distribution computed with Equation (2.6) can constrain M_ν .

In Figure 13 we report the neutrino masses as a function of the sign inversion positions predicted by the Takahashi2012 and Mead2020 models and the DEMNUni maps. The 1σ error bars have been estimated as follows: we generate 5000 Gaussian realisations of the DEMNUni maps and estimate the errors as the standard deviation of the 5000 cross-spectra obtained from them.

For relevant values of the neutrino mass ($M_\nu < 0.12$ eV at 95% C.L. [7]), we find differences between the Takahashi2012 and Mead2020 models and the DEMNUni simulations at the $\sim 1.5 - 2\sigma$ level. This implies that robust constraints on the neutrino mass via the sign inversion detection will require improving the nonlinear modelling. Furthermore, because of cosmic variance at the multipole range of interest (see Appendix B) the possibility of detecting ℓ_{inv} appears to be unlikely. Nevertheless, we expect to be able to disentangle different M_ν values via the estimation of the overall amplitude of the signal on very small cosmological scales. As shown in [37], the accuracy of future CMB surveys will improve the detection of the T-galaxy cross-spectrum on extremely large multipoles. In future works, we plan to investigate this possibility.

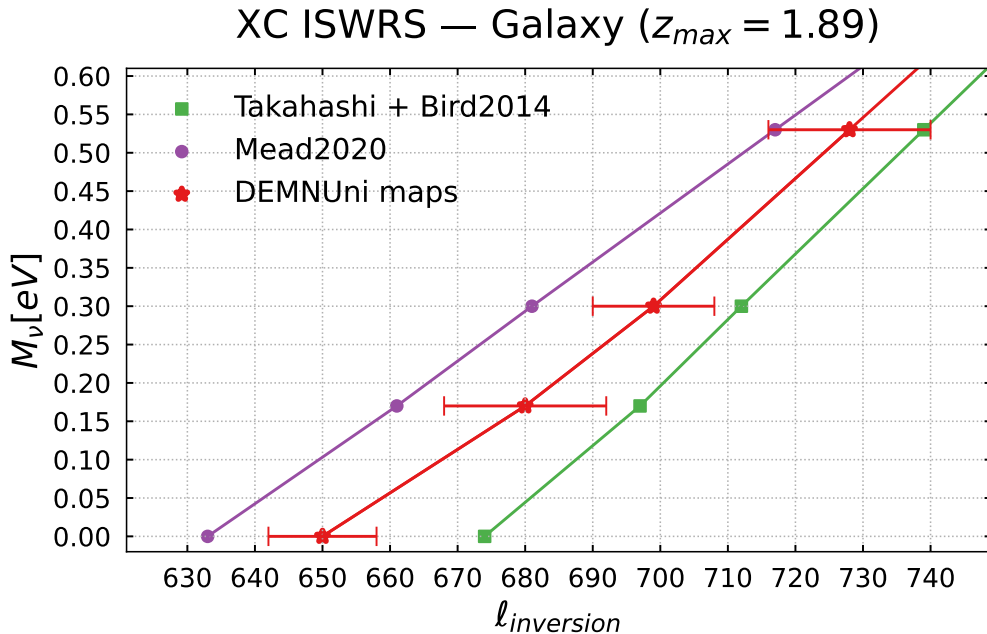


Figure 13: M_ν as a function of ℓ_{inv} . The green squares represent the result of ℓ_{inv} from Takahashi2012 model predictions with different cosmological scenarios, while the purple points are taken from Mead2020 model predictions. The red stars are the results of DEMNUni simulations. The error bars are estimated from Gaussian mocks.

5.3 Nonlinear ISWRS-galaxy cross-spectra: the case of different galaxy surveys

The last part of this work consists of computing predictions of the cross-spectra that can be observed on higher redshift ranges. First of all, we compute the ISWRS-galaxy distribution cross-power spectra that should be observable in a redshift range that goes up to $z = 2$, which is Euclid photometric range [27], setting $n(z)$ from Equation (3.2) with $z_m = 0.9$, shown in the upper panels of Figure 14. In the middle and bottom panels we report the cross-spectra obtained using the same $n(z)$, but with $z_m = 2, 3$ respectively (see Figure 6). Differently from all the previous theoretical spectra showed, here all the predictions have been computed integrating up to $z_{max} = 8$. It is evident at first glance that the higher is the redshift, the larger is the difference between the four M_ν values, with both the **Halofit** models considered so far. This is because the late Universe (i.e. small z) is characterised by the presence of DE, that affects the appearance of nonlinearities and is expected to have similar effects as

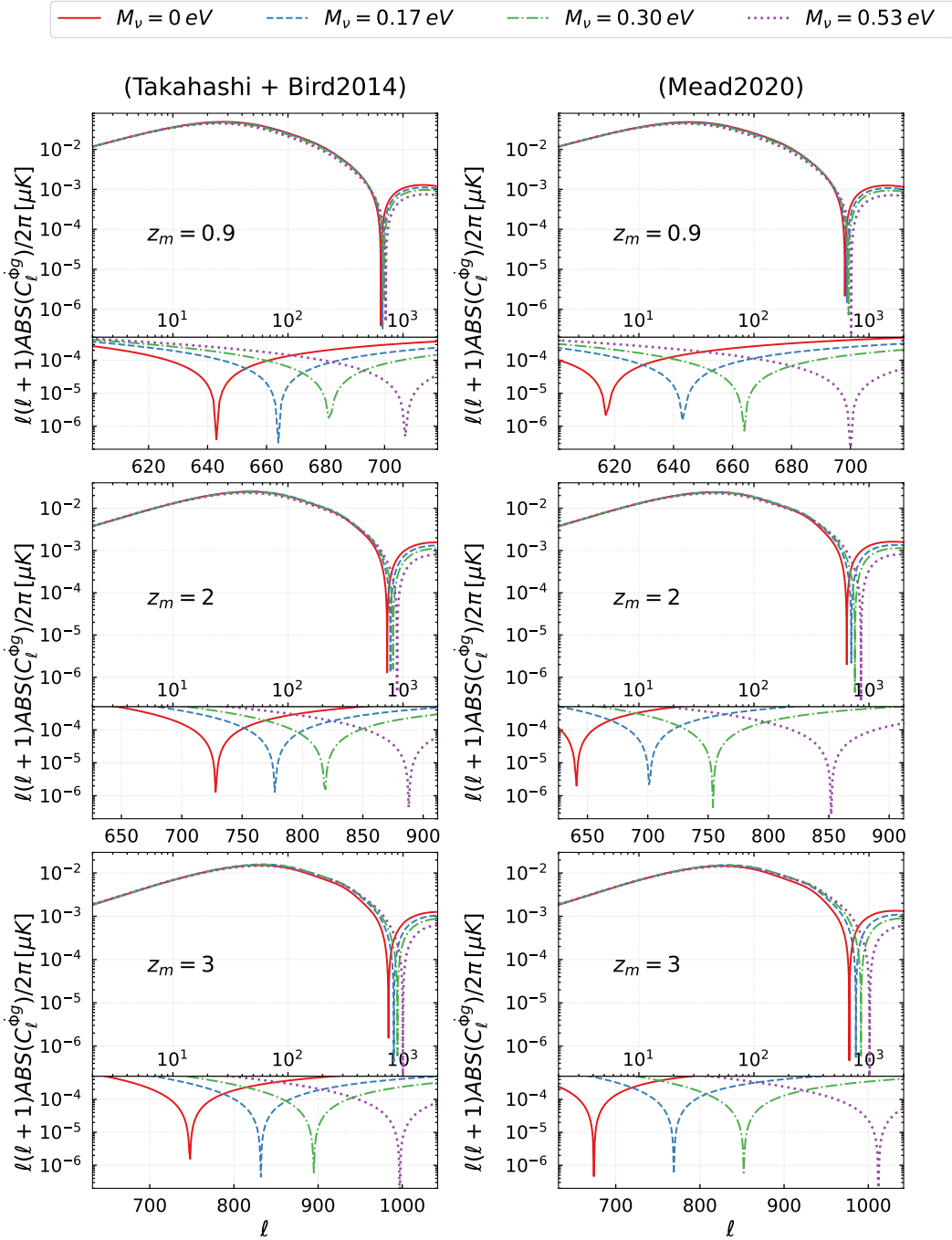


Figure 14: *Left:* Predictions of the ISWRS-galaxy cross-spectra for $M_\nu = 0, 0.17, 0.30, 0.53$ eV (solid red, dashed blue, dot-dashed green and dotted purple lines, respectively), computed with the Takahashi2012 model using: n_z from Equation (3.2) with $z_m = 0.9$ (*top panel*), which corresponds to the Euclid photometric survey, $z_m = 2$ (*centre panel*) and $z_m = 3$ (*bottom panel*). The subpanels of each plot show a zoom in of the sign inversion region. *Right:* Same as the left panels for the Mead2020 model.

neutrinos on this cross-spectrum. Hence, the further we go back in time, the less DE effects will be present, and the shift we measure will be due only to the mass of neutrinos.

6 Conclusions

The aim of this work is to develop an analytical modelling to reproduce the cross-power spectra of the ISWRS signal with the CMB-lensing potential and the galaxy distribution in the presence of massive neutrinos, validated via the DEMNUni simulations.

We consider both the linear (ISW) and nonlinear (RS) effects, i.e. we account also for the nonlinear regime where a sign inversion appears in the cross-spectra due to the anti-correlation between the RS effect and the CMB-lensing/galaxy-distribution. Moreover, the presence of massive neutrinos affects the position of this sign inversion, and specifically, the more neutrinos are massive, the more such a position shifts towards larger multipoles ℓ . This is because the more neutrinos are massive, the more they suppress the matter power spectrum, shifting the appearance of nonlinearities towards smaller cosmological scales.

There is already evidence of this effect at the level of the matter power spectra associated to these cross-correlations, $P_{\hat{\phi}\hat{\phi}}$ and $P_{\hat{\phi}\delta}$, as we show in Section 2. We compute them using two `Halofit` models implemented in `CAMB` (Takahashi2012+Bird2014 and Mead2020, which allow us to investigate also high redshifts), assuming a Planck-like baseline cosmology and adding neutrinos with $M_\nu = 0.17, 0.30, 0.53$ eV. We verify that a sign inversion appears in the transition from the linear to the nonlinear regime and that the presence of massive neutrinos affects its position. Moreover, we find that the lower the redshift is, the larger the scale where nonlinearities appear are, because the RS effect dominates over the late ISW one as we go back in time. Focusing on the nonlinear modelling, we find that Takahashi2012 predicts a higher level of nonlinearities with respect to Mead2020 at small redshifts, but this trend is inverted for $z \geq 1.1$ (see Figures 1 and 2).

The main results of this work is checking the presence of the same effects in the corresponding angular cross-power spectra, obtained from $P_{\hat{\phi}\hat{\phi}}$ and $P_{\hat{\phi}\delta}$, using Equation (2.5) and Equation (2.6).

Concerning the cross-correlation between the ISWRS signal and the CMB-lensing potential, we find that both DEMNUni maps and the theoretical predictions, computed using the Takahashi2012 and Mead2020 models, show the sign inversion due to the anti-correlation between the RS and the CMB-lensing, and the shift of this sign inversion towards larger multipoles as M_ν increases (see Figure 9).

Furthermore, we observe that, while the Mead2020 modelling tends to overestimate nonlinearities (and the sign inversions appear always on smaller multipoles with respect to DEMNUni mocks), the Takahashi2012 modelling gives different results depending on M_ν , and its sign inversions positions are extremely close to those of the simulations for $M_\nu = 0.17, 0.30$ eV.

The same results have been achieved for the cross-correlation between the ISWRS and the galaxy distribution with both DEMNUni maps and the theoretical predictions (see Figure 10). This represents an improvement with respect to [43], where only the massless neutrino case was investigated, and extends the work of [16] properly treating the impact of massive neutrinos on this cross-correlation in the nonlinear regime. We find that the Takahashi2012 models consistently underestimates nonlinearities compared to simulations, resulting in sign inversions occurring on smaller cosmological scales, i.e. larger multipoles. Conversely, the Mead2020 model overestimates nonlinearities. This could be due to the fact that such models

are not correctly able to recover the time variation of the gravitational potentials which give rise to the ISWRS effects.

Considering the dependence of this cross-correlation on galaxy bias, we have conducted two further tests to quantify the effects of different bias modellings. Firstly, we test how the analytical predictions may vary with respect to mock data when including in the calculation a bias that is specific to the massive neutrino cosmology, or simply the bias of the massless neutrino case. We observe that, when examining small values of M_ν , the difference between the massless and the massive neutrino bias functions is negligible (Figure 11). Conversely, when considering large values of M_ν , the difference cannot be neglected, and a bias model specific to that cosmology is required. However, in view of the fact that the most recent constraints on neutrino masses suggest $M_\nu < 0.12$ eV [7], a bias associated to a massless neutrino case cosmology would be appropriate to produce accurate forecasts. Secondly, we test different scale-independent and scale-dependent bias functions extracted from DEMNUni particle snapshots for the massless neutrino case. We verify that choosing a scale-dependent bias $b(k, z)$ results in spectra whose amplitudes better fit the mocks data, as suggested in [43], with both Takahashi2012 and Mead modellings (Figure 12). Overall in this work, we have developed an analytical method that exploits the Boltzmann solver code **CAMB**, and it has been validated against the DEMNUni simulations [18]. It is a powerful tool to investigate these cross-correlations without having to run large N-body simulations. Furthermore, thanks to the adaptability of **CAMB**, different cosmological scenarios can be easily tested.

The results highlight the strict connection between the sign inversion position and the value of neutrino masses. However, the need of sophisticated simulations to model nonlinearities makes it difficult to predict ℓ_{inv} , and cosmic variance makes it unlikely to detect it. Therefore, this method is not practical for estimating M_ν . We expect future surveys (i.e. CMB experiments such as The Simons Observatory [83], LiteBIRD[84], CMB-S4 [35] and galaxy surveys such as Euclid [27], The Roman Space telescope [85], the Vera Rubin Observatory [86]) to enable us to detect different amplitudes of these cross-spectra on very small scales depending on the value of M_ν . We intend to extend the work of [37] to massive neutrino cases to verify this hypothesis.

Finally, we have verified that these cross-spectra differ at various redshifts because of the different role played by DE. A straightforward extension would be to include DDE models in this analysis. The study of the DE EoS dependency of the ISWRS cross-spectra with LSS tracers could help to distinguish between different DE models, and this analysis could provide insights on the properties and the evolution of DE. We expect to extend the present analysis to the case of DDE models in the next future.

Acknowledgments

VC and MM are partially supported by the INFN project “InDark”. MC is partially supported by a 2021/22 “Research and Education” grant from Fondazione CRT. The OAVdA is managed by the Fondazione Clément Fillietroz-ONLUS, which is supported by the Regional Government of the Aosta Valley, the Town Municipality of Nus and the “Unité des Communes valdôtaines Mont-Émilis”. The DEMNUni simulations were carried out in the framework of “The Dark Energy and Massive-Neutrino Universe” project, using the Tier-0 IBM BG/Q Fermi machine and the Tier-0 Intel OmniPath Cluster Marconi-A1 of the Centro Interuniversitario del Nord-Est per il Calcolo Elettronico (CINECA). We acknowledge a generous CPU and storage allocation by the Italian Super-Computing Resource Allocation

(IS CRA) as well as from the coordination of the “Accordo Quadro MoU per lo svolgimento di attività congiunta di ricerca Nuove frontiere in Astrofisica: HPC e Data Exploration di nuova generazione”, together with storage from INFN-CNAF and INAF-IA2.

References

- [1] A.A. Penzias and R.W. Wilson, *A Measurement of Excess Antenna Temperature at 4080 Mc/s.*, *ApJ* **142** (1965) 419.
- [2] C.L. Bennett, M. Halpern, G. Hinshaw, N. Jarosik, A. Kogut, M. Limon et al., *First-Year Wilkinson Microwave Anisotropy Probe (WMAP) Observations: Preliminary Maps and Basic Results*, *ApJS* **148** (2003) 1 [[astro-ph/0302207](#)].
- [3] D.N. Spergel, L. Verde, H.V. Peiris, E. Komatsu, M.R. Nolta, C.L. Bennett et al., *First-Year Wilkinson Microwave Anisotropy Probe (WMAP) Observations: Determination of Cosmological Parameters*, *ApJS* **148** (2003) 175 [[astro-ph/0302209](#)].
- [4] E. Komatsu, K.M. Smith, J. Dunkley, C.L. Bennett, B. Gold, G. Hinshaw et al., *Seven-year Wilkinson Microwave Anisotropy Probe (WMAP) Observations: Cosmological Interpretation*, *ApJS* **192** (2011) 18 [[1001.4538](#)].
- [5] Planck Collaboration, P.A.R. Ade, N. Aghanim, C. Armitage-Caplan, M. Arnaud, M. Ashdown et al., *Planck 2013 results. XVI. Cosmological parameters*, *A&A* **571** (2014) A16 [[1303.5076](#)].
- [6] Planck Collaboration, P.A.R. Ade, N. Aghanim, M. Arnaud, M. Ashdown, J. Aumont et al., *Planck 2015 results. XIII. Cosmological parameters*, *A&A* **594** (2016) A13 [[1502.01589](#)].
- [7] Planck Collaboration, N. Aghanim, Y. Akrami, M. Ashdown, J. Aumont, C. Baccigalupi et al., *Planck 2018 results. VI. Cosmological parameters*, *A&A* **641** (2020) A6 [[1807.06209](#)].
- [8] E.V. Linder, *Exploring the Expansion History of the Universe*, *Phys. Rev. Lett.* **90** (2003) 091301 [[astro-ph/0208512](#)].
- [9] J. Lesgourgues and S. Pastor, *Neutrino mass from Cosmology*, *arXiv e-prints* (2012) arXiv:1212.6154 [[1212.6154](#)].
- [10] M. Archidiacono, S. Hannestad and J. Lesgourgues, *What will it take to measure individual neutrino mass states using cosmology?*, *J. Cosmology Astropart. Phys.* **2020** (2020) 021 [[2003.03354](#)].
- [11] R.K. Sachs and A.M. Wolfe, *Perturbations of a Cosmological Model and Angular Variations of the Microwave Background*, *ApJ* **147** (1967) 73.
- [12] M.J. Rees and D.W. Sciama, *Large-scale Density Inhomogeneities in the Universe*, *Nature* **217** (1968) 511.
- [13] J.R. Bond, G. Efstathiou and J. Silk, *Massive neutrinos and the large-scale structure of the universe*, *Phys. Rev. Lett.* **45** (1980) 1980.
- [14] R.G. Crittenden and N. Turok, *Looking for a Cosmological Constant with the Rees-Sciama Effect*, *Phys. Rev. Lett.* **76** (1996) 575 [[astro-ph/9510072](#)].
- [15] T. Giannantonio, R. Scranton, R.G. Crittenden, R.C. Nichol, S.P. Boughn, A.D. Myers et al., *Combined analysis of the integrated Sachs-Wolfe effect and cosmological implications*, *Phys. Rev. D* **77** (2008) 123520 [[0801.4380](#)].
- [16] J. Lesgourgues, W. Valkenburg and E. Gaztañaga, *Constraining neutrino masses with the integrated-Sachs-Wolfe-galaxy correlation function*, *Phys. Rev. D* **77** (2008) 063505 [[0710.5525](#)].
- [17] Y.-C. Cai, S. Cole, A. Jenkins and C. Frenk, *Towards accurate modelling of the integrated Sachs-Wolfe effect: the non-linear contribution*, *MNRAS* **396** (2009) 772 [[0809.4488](#)].

- [18] C. Carbone, M. Petkova and K. Dolag, *DEMNUi: ISW, Rees-Sciama, and weak-lensing in the presence of massive neutrinos*, *J. Cosmology Astropart. Phys.* **2016** (2016) 034 [[1605.02024](#)].
- [19] A. Lewis and A. Challinor, “CAMB: Code for Anisotropies in the Microwave Background.” Astrophysics Source Code Library, record ascl:1102.026, Feb., 2011.
- [20] R.E. Smith, J.A. Peacock, A. Jenkins, S.D.M. White, C.S. Frenk, F.R. Pearce et al., *Stable clustering, the halo model and non-linear cosmological power spectra*, *MNRAS* **341** (2003) 1311 [[astro-ph/0207664](#)].
- [21] R. Takahashi, M. Sato, T. Nishimichi, A. Taruya and M. Oguri, *Revising the Halofit Model for the Nonlinear Matter Power Spectrum*, *ApJ* **761** (2012) 152 [[1208.2701](#)].
- [22] S. Bird, M. Viel and M.G. Haehnelt, *Massive neutrinos and the non-linear matter power spectrum*, *MNRAS* **420** (2012) 2551 [[1109.4416](#)].
- [23] A.J. Mead, S. Brieden, T. Tröster and C. Heymans, *HMCODE-2020: improved modelling of non-linear cosmological power spectra with baryonic feedback*, *MNRAS* **502** (2021) 1401 [[2009.01858](#)].
- [24] A.J. Mead, J.A. Peacock, C. Heymans, S. Joudaki and A.F. Heavens, *An accurate halo model for fitting non-linear cosmological power spectra and baryonic feedback models*, *MNRAS* **454** (2015) 1958 [[1505.07833](#)].
- [25] R. Laureijs, J. Amiaux, S. Arduini, J.L. Auguères, J. Brinchmann, R. Cole et al., *Euclid Definition Study Report*, *arXiv e-prints* (2011) [arXiv:1110.3193](#) [[1110.3193](#)].
- [26] Euclid Collaboration, A. Blanchard, S. Camera, C. Carbone, V.F. Cardone, S. Casas et al., *Euclid preparation. VII. Forecast validation for Euclid cosmological probes*, *A&A* **642** (2020) A191 [[1910.09273](#)].
- [27] Euclid Collaboration, R. Scaramella, J. Amiaux, Y. Mellier, C. Burigana, C.S. Carvalho et al., *Euclid preparation. I. The Euclid Wide Survey*, *A&A* **662** (2022) A112 [[2108.01201](#)].
- [28] M. Santos, P. Bull, D. Alonso, S. Camera, P. Ferreira, G. Bernardi et al., *Cosmology from a SKA HI intensity mapping survey*, in *Advancing Astrophysics with the Square Kilometre Array (AASKA14)*, p. 19, Apr., 2015, DOI [[1501.03989](#)].
- [29] D. Kirk, F.B. Abdalla, A. Benoit-Lévy, P. Bull and B. Joachimi, *Cross correlation surveys with the Square Kilometre Array*, in *Advancing Astrophysics with the Square Kilometre Array (AASKA14)*, p. 20, Apr., 2015, DOI [[1501.03848](#)].
- [30] I. Harrison, S. Camera, J. Zuntz and M.L. Brown, *SKA weak lensing - I. Cosmological forecasts and the power of radio-optical cross-correlations*, *MNRAS* **463** (2016) 3674 [[1601.03947](#)].
- [31] S. Camera, A. Raccanelli, P. Bull, D. Bertacca, X. Chen, P. Ferreira et al., *Cosmology on the Largest Scales with the SKA*, in *Advancing Astrophysics with the Square Kilometre Array (AASKA14)*, p. 25, Apr., 2015, DOI [[1501.03851](#)].
- [32] M. Brown, D. Bacon, S. Camera, I. Harrison, B. Joachimi, R.B. Metcalf et al., *Weak gravitational lensing with the Square Kilometre Array*, in *Advancing Astrophysics with the Square Kilometre Array (AASKA14)*, p. 23, Apr., 2015, DOI [[1501.03828](#)].
- [33] A. Weltman, P. Bull, S. Camera, K. Kelley, H. Padmanabhan, J. Pritchard et al., *Fundamental physics with the Square Kilometre Array*, *PASA* **37** (2020) e002 [[1810.02680](#)].
- [34] D.J. Schwarz, D. Bacon, S. Chen, C. Clarkson, D. Huterer, M. Kunz et al., *Testing foundations of modern cosmology with SKA all-sky surveys*, in *Advancing Astrophysics with the Square Kilometre Array (AASKA14)*, p. 32, Apr., 2015, DOI [[1501.03820](#)].
- [35] K.N. Abazajian, P. Adshead, Z. Ahmed, S.W. Allen, D. Alonso, K.S. Arnold et al., *CMB-S4 Science Book, First Edition*, *arXiv e-prints* (2016) [arXiv:1610.02743](#) [[1610.02743](#)].

- [36] K. Abazajian, A. Abdulghafour, G.E. Addison, P. Adshead, Z. Ahmed, M. Ajello et al., *Snowmass 2021 CMB-S4 White Paper*, *arXiv e-prints* (2022) arXiv:2203.08024 [2203.08024].
- [37] S. Ferraro, E. Schaane and E. Pierpaoli, *Is the Rees-Sciama effect detectable by the next generation of cosmological experiments?*, *arXiv e-prints* (2022) arXiv:2205.10332 [2205.10332].
- [38] T. Giannantonio, R. Crittenden, R. Nichol and A.J. Ross, *The significance of the integrated Sachs-Wolfe effect revisited*, *MNRAS* **426** (2012) 2581 [1209.2125].
- [39] Y.-C. Cai, S. Cole, A. Jenkins and C.S. Frenk, *Full-sky map of the ISW and Rees-Sciama effect from Gpc simulations*, *MNRAS* **407** (2010) 201 [1003.0974].
- [40] G. Rossi, N. Palanque-Delabrouille, A. Borde, M. Viel, C. Yèche, J.S. Bolton et al., *Suite of hydrodynamical simulations for the Lyman- α forest with massive neutrinos*, *A&A* **567** (2014) A79 [1401.6464].
- [41] A.J. Nishizawa, E. Komatsu, N. Yoshida, R. Takahashi and N. Sugiyama, *Cosmic Microwave Background-Weak Lensing Correlation: Analytical and Numerical Study of Nonlinearity and Implications for Dark Energy*, *ApJ* **676** (2008) L93 [0711.1696].
- [42] U. Seljak, *Rees-Sciama Effect in a Cold Dark Matter Universe*, *ApJ* **460** (1996) 549 [astro-ph/9506048].
- [43] R.E. Smith, C. Hernández-Monteagudo and U. Seljak, *Impact of scale dependent bias and nonlinear structure growth on the integrated Sachs-Wolfe effect: Angular power spectra*, *Phys. Rev. D* **80** (2009) 063528 [0905.2408].
- [44] A. Mangilli and L. Verde, *Non-Gaussianity and the CMB bispectrum: Confusion between primordial and lensing-Rees-Sciama contribution?*, *Phys. Rev. D* **80** (2009) 123007 [0906.2317].
- [45] E. Castorina, C. Carbone, J. Bel, E. Sefusatti and K. Dolag, *DEMNUi: the clustering of large-scale structures in the presence of massive neutrinos*, *J. Cosmology Astropart. Phys.* **2015** (2015) 043 [1505.07148].
- [46] M. Moresco, F. Marulli, L. Moscardini, E. Branchini, A. Cappi, I. Davidzon et al., *The VIMOS Public Extragalactic Redshift Survey (VIPERS) . Exploring the dependence of the three-point correlation function on stellar mass and luminosity at $0.5 < z < 1.1$* , *A&A* **604** (2017) A133 [1603.08924].
- [47] M. Zennaro, J. Bel, J. Dossett, C. Carbone and L. Guzzo, *Cosmological constraints from galaxy clustering in the presence of massive neutrinos*, *MNRAS* **477** (2018) 491 [1712.02886].
- [48] R. Ruggeri, E. Castorina, C. Carbone and E. Sefusatti, *DEMNUi: massive neutrinos and the bispectrum of large scale structures*, *J. Cosmology Astropart. Phys.* **2018** (2018) 003 [1712.02334].
- [49] J. Bel, A. Pezzotta, C. Carbone, E. Sefusatti and L. Guzzo, *Accurate fitting functions for peculiar velocity spectra in standard and massive-neutrino cosmologies*, *A&A* **622** (2019) A109 [1809.09338].
- [50] G. Parimbelli, S. Anselmi, M. Viel, C. Carbone, F. Villaescusa-Navarro, P.S. Corasaniti et al., *The effects of massive neutrinos on the linear point of the correlation function*, *J. Cosmology Astropart. Phys.* **2021** (2021) 009 [2007.10345].
- [51] G. Parimbelli, C. Carbone, J. Bel, B. Bose, M. Calabrese, E. Carella et al., *DEMNUi: comparing nonlinear power spectra prescriptions in the presence of massive neutrinos and dynamical dark energy*, *J. Cosmology Astropart. Phys.* **2022** (2022) 041 [2207.13677].
- [52] P. Baratta, J. Bel, S. Gouyou Beauchamps and C. Carbone, *COVMOS: a new Monte Carlo approach for galaxy clustering analysis*, *arXiv e-prints* (2022) arXiv:2211.13590 [2211.13590].
- [53] M. Guidi, A. Veropalumbo, E. Branchini, A. Eggemeier and C. Carbone, *Modelling the*

- next-to-leading order matter three-point correlation function using FFTLog*, *arXiv e-prints* (2022) [arXiv:2212.07382](#) [[2212.07382](#)].
- [54] S. Gouyou Beauchamps, P. Baratta, S. Escoffier, W. Gillard, J. Bel, J. Bautista et al., *Cosmological inference including massive neutrinos from the matter power spectrum: biases induced by uncertainties in the covariance matrix*, *arXiv e-prints* (2023) [arXiv:2306.05988](#) [[2306.05988](#)].
- [55] E. Carella, C. Carbone, M. Zennaro, G. Girelli, M. Bolzonella, F. Marulli et al., *DEMNUi: The galaxy-halo connection in the presence of dynamical dark energy and massive neutrinos*, *In prep*.
- [56] M. Roncarelli, C. Carbone and L. Moscardini, *The effect of massive neutrinos on the Sunyaev-Zel'dovich and X-ray observables of galaxy clusters*, *MNRAS* **447** (2015) 1761 [[1409.4285](#)].
- [57] G. Fabbian, M. Calabrese and C. Carbone, *CMB weak-lensing beyond the Born approximation: a numerical approach*, *J. Cosmology Astropart. Phys.* **2018** (2018) 050 [[1702.03317](#)].
- [58] B. Hernández-Molinero, C. Carbone, R. Jimenez and C. Peña Garay, *Cosmic Background Neutrinos Deflected by Gravity: DEMNUi Simulation Analysis*, *arXiv e-prints* (2023) [arXiv:2301.12430](#) [[2301.12430](#)].
- [59] C.D. Kreisch, A. Pisani, C. Carbone, J. Liu, A.J. Hawken, E. Massara et al., *Massive neutrinos leave fingerprints on cosmic voids*, *MNRAS* **488** (2019) 4413 [[1808.07464](#)].
- [60] N. Schuster, N. Hamaus, A. Pisani, C. Carbone, C.D. Kreisch, G. Pollina et al., *The bias of cosmic voids in the presence of massive neutrinos*, *J. Cosmology Astropart. Phys.* **2019** (2019) 055 [[1905.00436](#)].
- [61] G. Verza, A. Pisani, C. Carbone, N. Hamaus and L. Guzzo, *The void size function in dynamical dark energy cosmologies*, *J. Cosmology Astropart. Phys.* **2019** (2019) 040 [[1906.00409](#)].
- [62] G. Verza, C. Carbone and A. Renzi, *The Halo Bias inside Cosmic Voids*, *ApJ* **940** (2022) L16 [[2207.04039](#)].
- [63] G. Verza, C. Carbone, A. Pisani and A. Renzi, *DEMNUi: disentangling dark energy from massive neutrinos with the void size function*, *arXiv e-prints* (2022) [arXiv:2212.09740](#) [[2212.09740](#)].
- [64] P. Vielzeuf, M. Calabrese, C. Carbone, G. Fabbian and C. Baccigalupi, *DEMNUi: The imprint of massive neutrinos on the cross-correlation between cosmic voids and CMB lensing*, *arXiv e-prints* (2023) [arXiv:2303.10048](#) [[2303.10048](#)].
- [65] M. Zennaro, J. Bel, F. Villaescusa-Navarro, C. Carbone, E. Sefusatti and L. Guzzo, *Initial conditions for accurate N-body simulations of massive neutrino cosmologies*, *MNRAS* **466** (2017) 3244 [[1605.05283](#)].
- [66] V. Springel, *The cosmological simulation code GADGET-2*, *MNRAS* **364** (2005) 1105 [[astro-ph/0505010](#)].
- [67] M. Viel, M.G. Haehnelt and V. Springel, *The effect of neutrinos on the matter distribution as probed by the intergalactic medium*, *J. Cosmology Astropart. Phys.* **2010** (2010) 015 [[1003.2422](#)].
- [68] K.M. Górski, E. Hivon, A.J. Banday, B.D. Wandelt, F.K. Hansen, M. Reinecke et al., *HEALPix: A Framework for High-Resolution Discretization and Fast Analysis of Data Distributed on the Sphere*, *ApJ* **622** (2005) 759 [[astro-ph/0409513](#)].
- [69] C. Carbone, V. Springel, C. Baccigalupi, M. Bartelmann and S. Matarrese, *Full-sky maps for gravitational lensing of the cosmic microwave background*, *MNRAS* **388** (2008) 1618 [[0711.2655](#)].

- [70] B.M. Schäfer and M. Bartelmann, *Weak lensing in the second post-Newtonian approximation: gravitomagnetic potentials and the integrated Sachs-Wolfe effect*, *MNRAS* **369** (2006) 425 [[astro-ph/0502208](#)].
- [71] B.M. Schäfer, *Mixed three-point correlation functions of the non-linear integrated Sachs-Wolfe effect and their detectability*, *MNRAS* **388** (2008) 1394 [[0803.1095](#)].
- [72] M. Calabrese, C. Carbone, G. Fabbian, M. Baldi and C. Baccigalupi, *Multiple lensing of the cosmic microwave background anisotropies*, *J. Cosmology Astropart. Phys.* **2015** (2015) 049 [[1409.7680](#)].
- [73] P. Fosalba, E. Gaztañaga, F.J. Castander and M. Manera, *The onion universe: all sky lightcone simulations in spherical shells*, *MNRAS* **391** (2008) 435 [[0711.1540](#)].
- [74] S. Hilbert, A. Barreira, G. Fabbian, P. Fosalba, C. Giocoli, S. Bose et al., *The accuracy of weak lensing simulations*, *MNRAS* **493** (2020) 305 [[1910.10625](#)].
- [75] B.P. Moster, R.S. Somerville, C. Maubetsch, F.C. Van den Bosch, A.V. Macciò, T. Naab et al., *Constraints on the relationship between stellar mass and halo mass at low and high redshift*, *ApJ* **710** (2010) 903 [[0903.4682](#)].
- [76] F. Shankar, A. Lapi, P. Salucci, G. De Zotti and L. Danese, *New Relationships between Galaxy Properties and Host Halo Mass, and the Role of Feedbacks in Galaxy Formation*, *ApJ* **643** (2006) 14 [[astro-ph/0601577](#)].
- [77] G. Girelli, L. Pozzetti, M. Bolzonella, C. Giocoli, F. Marulli and M. Baldi, *The stellar-to-halo mass relation over the past 12 Gyr. I. Standard Λ CDM model*, *A&A* **634** (2020) A135 [[2001.02230](#)].
- [78] I. Tutusaus, M. Martinelli, V.F. Cardone, S. Camera, S. Yahia-Cherif, S. Casas et al., *Euclid: The importance of galaxy clustering and weak lensing cross-correlations within the photometric Euclid survey*, *A&A* **643** (2020) A70 [[2005.00055](#)].
- [79] C. Modi, S.-F. Chen and M. White, *Simulations and symmetries*, *MNRAS* **492** (2020) 5754 [[1910.07097](#)].
- [80] M. Calabrese, C. Carbone, E. Carella et al., *Mock simulations for cmb cross-correlation (in prep.)*, .
- [81] F. Marulli, C. Carbone, M. Viel, L. Moscardini and A. Cimatti, *Effects of massive neutrinos on the large-scale structure of the Universe*, *MNRAS* **418** (2011) 346 [[1103.0278](#)].
- [82] L. Xu, *Probing the neutrino mass through the cross correlation between the Rees-Sciama effect and weak lensing*, *J. Cosmology Astropart. Phys.* **2016** (2016) 059 [[1605.02403](#)].
- [83] A. Lee, M.H. Abitbol and S. Adachi et al., *The Simons Observatory*, in *Bulletin of the American Astronomical Society*, vol. 51, p. 147, Sept., 2019 [[1907.08284](#)].
- [84] LiteBIRD Collaboration, E. Allys, K. Arnold, J. Aumont, R. Aurlen, S. Azzoni et al., *Probing cosmic inflation with the LiteBIRD cosmic microwave background polarization survey*, *Progress of Theoretical and Experimental Physics* **2023** (2023) 042F01 [[2202.02773](#)].
- [85] T. Eifler, H. Miyatake, E. Krause, C. Heinrich, V. Miranda, C. Hirata et al., *Cosmology with the Roman Space Telescope - multiprobe strategies*, *MNRAS* **507** (2021) 1746 [[2004.05271](#)].
- [86] Ž. Ivezić, S.M. Kahn and J.A.T. et al., *LSST: From science drivers to reference design and anticipated data products*, *The Astrophysical Journal* **873** (2019) 111.
- [87] U. Seljak, N. Hamaus and V. Desjacques, *How to Suppress the Shot Noise in Galaxy Surveys*, *Phys. Rev. Lett.* **103** (2009) 091303 [[0904.2963](#)].

A Test nonlinearities in the dark matter power spectra

As showed in Section 2 (Figure 1 and Figure 2), there are inaccuracies in the Takahashi2012 nonlinear model in the representation of both $P_{\dot{\Phi}\Phi}$ and $P_{\dot{\Phi}\delta}$ at $z = 0.5$, where the sign inversion for the $M_\nu = 0.17$ eV case occurs at larger multipoles than the massless neutrino one. We decided then to analyse the trend of both Takahashi2012 and Mead2020 model for masses close to 0.17 eV to check possible irregularities. The results are shown in Figure 15 for $P_{\dot{\Phi}\Phi}$ and in Figure 16 for $P_{\dot{\Phi}\delta}$. It is easy to notice how neither Takahashi2012 nor Mead2020 are able to reproduce the expected trend in the ℓ_{inv} position for all M_ν at all redshifts. An improvement in the Halofit models is then required to correctly represent these signals.

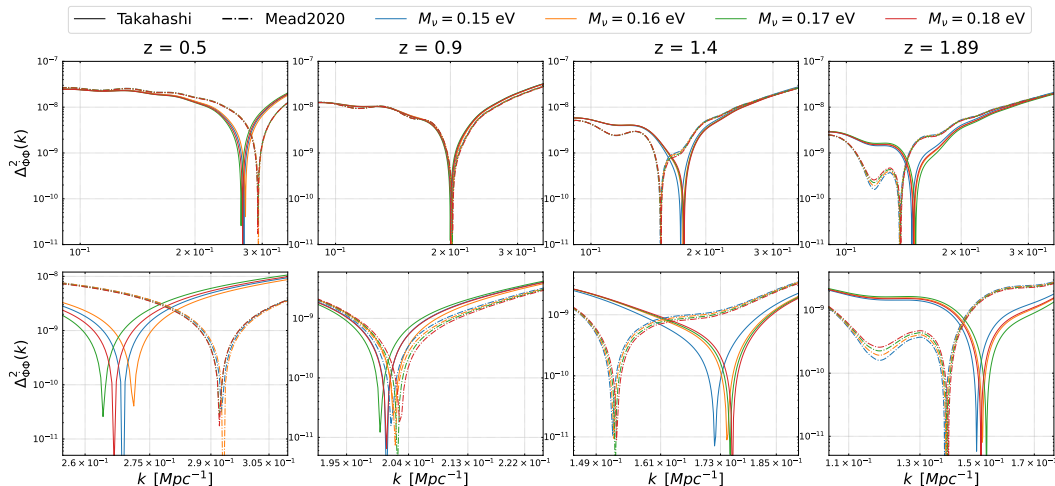


Figure 15: *Top:* Dimensionless and scaled form of the ISWRS–CMB-lensing potential cross-spectra as a function of the wavenumber k at $z = 0.5, 0.9, 1.4, 1.89$ for $M_\nu = 0.15, 0.16, 0.17, 0.18$ eV (blue, yellow, green and red lines, respectively), obtained via the Takahashi2012 model (solid lines) and the Mead2020 model (dashed lines). *Bottom:* Zoom of the top panels on the sign inversions.

B Cosmic Variance (massless neutrino case)

We assess the uncertainty associated to the cross-spectra in terms of cosmic variance [16, 87]:

$$\sigma_{C_\ell} = \sqrt{\frac{2(C_\ell)^2}{2\ell + 1}}. \quad (\text{B.1})$$

For the computation of the cosmic variance of the cross-correlation of the ISWRS signal with the CMB-lensing potential and the galaxy distribution, we divide the signal variance (σ) in logarithmic equispaced bins $\Delta\ell_{bin_i}$:

$$\sigma_{C_\ell^{\dot{\Phi}\Phi}, bin_i} = \sqrt{\frac{(C_\ell^{\dot{\Phi}\Phi})^2 + C_\ell^{TT} C_\ell^{\dot{\Phi}\Phi}}{(2\ell + 1)\Delta\ell_{bin_i}}}, \quad (\text{B.2})$$

$$\sigma_{C_\ell^{\dot{\Phi}g}, bin_i} = \sqrt{\frac{(C_\ell^{\dot{\Phi}g})^2 + C_\ell^{TT}(C_\ell^{gg} + N_{gg})}{(2\ell + 1)\Delta\ell_{bin_i}}}. \quad (\text{B.3})$$

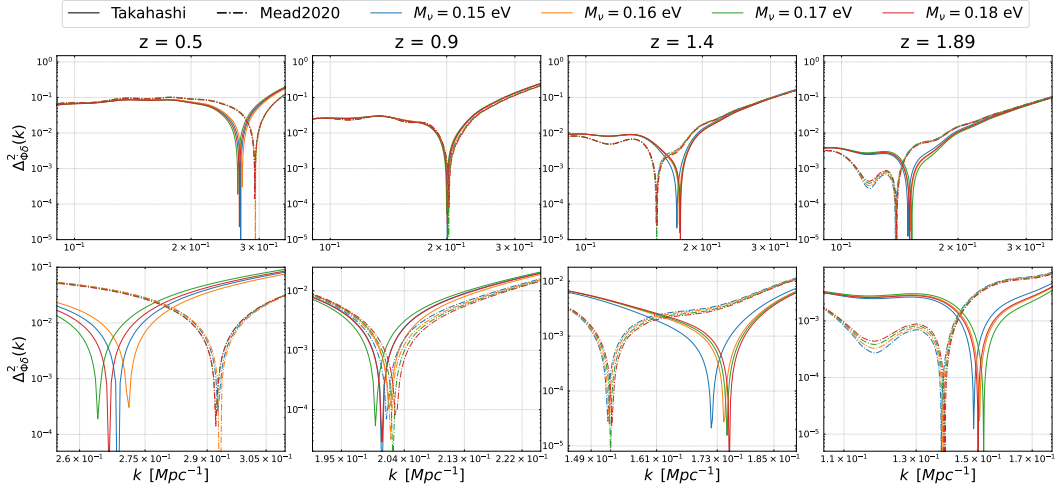


Figure 16: *Top:* Dimensionless and scaled form of the ISWRS–galaxy distribution cross-spectra as a function of the wavenumber k at $z = 0.5, 0.9, 1.4, 1.89$ for $M_\nu = 0.15, 0.16, 0.17, 0.18$ eV (blue, yellow, green and red lines, respectively), obtained via the Takahashi2012 model (solid lines) and the Mead2020 model (dashed lines). *Bottom:* Zoom of the top panels on the sign inversions.

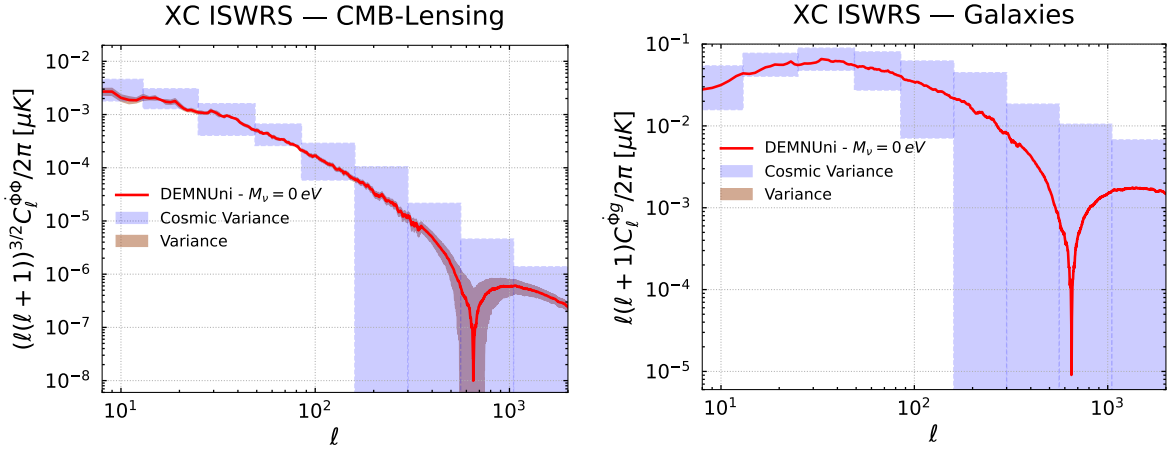


Figure 17: *Left:* ISWRS–CMB-lensing potential cross-spectrum for $M_\nu = 0$ eV (red line) with its cosmic variance binned in fourteen logarithmic equispaced intervals (shaded blue area) and the variance obtained as the standard deviation of the 5000 realisations computed (shaded brown area). *Right:* Same as left, but for the ISWRS–galaxy cross-spectrum for $M_\nu = 0$ eV. In both panels, because of the choice to represent signals in range $\ell = [10, 2000]$, only eleven bins are shown.

The C_ℓ^{TT} that appears in Equation (B.2) and Equation (B.3) is the auto-power spectrum of CMB temperature primary anisotropies. Working with C_ℓ^{TT} instead of $C_\ell^{\delta\phi}$ arises from the fact that any CMB measurement is dominated by primary anisotropies, which are the main obstacle for a correct reconstruction of the ISWRS signal, and of secondary anisotropies in general. The N^{gg} term in Equation (B.3) is the shot-noise spectrum, given by Equation (??).

In this analysis, only the cosmic variance for the massless neutrino case of both the cross-spectra analysed has been computed. Moreover, we compared it with the standard deviation of 5000 realisations we computed for the two signals. Results are shown in Figure 17. The significant difference between the cosmic variance and the mocks variance is due to the fact that the 5000 gaussian realizations represent the same sky realization of the mocks, and consequently their scatter is small. Anyway, it is easy to notice that, in both panels, the larger variance values are in the larger multipole range, therefore the detection of ℓ_{inv} is highly unlikely.